A comprehensive analysis of multi-scale field aligned currents: Characteristics, controlling parameters, and relationships

Ryan M. McGranaghan[1,2], Anthony J. Mannucci[2], Colin Forsyth[3]

Ryan M. McGranaghan, ryan.mcgranaghan@jpl.nasa.gov

[1]University Corporation for Atmospheric Research (UCAR), Boulder, CO, 80301, USA.

[2]NASA Jet Propulsion Laboratory, California Institute of Technology, Pasadena, CA, 91109, USA.

[3]Mullard Space Science Laboratory, University College London, Dorking, UK.

This article has been accepted for publication and undergone full peer review but has not been through the copyediting, typesetting, pagination and proofreading process, which may lead to differences between this version and the Version of Record. Please cite this article as doi: 10.1002/2017JA024742

Abstract.

We explore the characteristics, controlling parameters, and relationships of multi-scale field aligned currents (FACs) using a rigorous, comprehensive, and cross-platform analysis. Our unique approach combines FAC data from the Swarm satellites and the Advanced Magnetosphere and Planetary Electrodynamics Response Experiment (AMPERE) to create a database of small-scale (∼10-150 km, <1° latitudinal width), mesoscale (∼150-250 km, 1-2° latitudinal width), and large-scale (>250 km) FACs. We examine these data for the repeatable behavior of FACs across scales (i.e., the characteristics), the dependence on the interplanetary magnetic field (IMF) orientation, and the degree to which each scale 'departs' from nominal large-scale specification. We retrieve new information by utilizing magnetic latitude and local time dependence, correlation analyses, and quantification of the departure of smaller from larger scales. We find that: 1) FACs characteristics and dependence on controlling parameters do not map between scales in a straight forward manner; 2) relationships between FAC scales exhibit local time dependence; and 3) the dayside high-latitude region is characterized by remarkably distinct FAC behavior when analyzed at different scales, and the locations of distinction correspond to 'anomalous' ionosphere-thermosphere (IT) behavior. Comparing with nominal large-scale FACs, we find that differences are characterized by a horseshoe shape, maximizing across dayside local times, and that difference magnitudes increase when smaller scale observed FACs are considered. We suggest that both new physics and increased resolution

of models are required to address the multi-scale complexities. We include a summary table of our findings to provide a quick reference for differences between multi-scale FACs.

Keypoints:

- Multi-scale FACs exhibit strong local time and interplanetary magnetic field orientation dependence
- FAC characteristics and dependence on controlling parameters do not map trivially across scales
- Differences between observed multi-scale and nominal large-scale FACs characterized by horseshoe shape in local time, maximizing on dayside

1. Introduction

Field-aligned currents (FACs), or the system of currents flowing along Earth's magnetic field lines are the dominant form of energy and momentum exchange between the magnetosphere and ionosphere and are critical to understanding the entire solar wind to magnetosphere-ionosphere-thermosphere (MIT) coupling. The existence of such a system of currents electrodynamically linking the magnetosphere and ionosphere was hypothesized at the turn of the twentieth century [*Birkeland*, 1908, 1913]. By the end of the 1970s the large-scale morphological features of these FACs had been established primarily through the magnetic perturbations produced at low Earth orbital altitudes [*Zmuda et al.*, 1966; *Iijima and Potemra*, 1976a, b, 1978].

Iijima and Potemra [1978] determined that the global average FACs consist of two concentric rings at ionospheric auroral altitudes: a poleward ring (Region 1, R1) and an equatorward ring (Region 2, R2). R1 and R2 currents are driven by different magnetospheric regions where R1 FACs are associated with the divergence of Chapman-Ferraro currents in the magnetopause and R2 FACs with the divergence of the partial ring current in the inner magnetosphere [*Cowley*, 2013]. R1 FACs flow into the ionosphere (downward current) at dawn local times (LTs) and out (upward current) at dusk LTs and the R2 FACs exhibit opposite polarities in each LT sector. The R1 currents are located where antisunward plasma flow across the polar cap interacts with sunward return flow at lower latitudes [*Dungey*, 1961]. The dynamics of the R1/R2 currents are, therefore, strongly tied to the Dungey convection cycle and magnetospheric activity. In the ionosphere the

R1/R2 currents close via Pedersen horizontal currents. Figure 1, reproduced from *Carter et al.* [2016], schematically depicts the system.

In recent decades much progress has been made in understanding the characteristics and controlling factors of the large-scale R1/R2 FACs [*Weimer*, 2001; *Ohtani et al.*, 2005; *Wang et al.*, 2005; *Anderson et al.*, 2008; *Juusola et al.*, 2009; *Coxon et al.*, 2014a, b; *Clausen et al.*, 2012; *Milan et al.*, 2015; *Carter et al.*, 2016; *Coxon et al.*, 2016, and references therein]. The distribution of FACs at the top of the ionosphere is determined by the electromagnetic coupling between the magnetosphere and the ionosphere, which, in turn, is controlled by the ionospheric conductivity [*McGranaghan*, 2016]. Conductivity depends primarily on two factors: 1) the solar radiation, through the ionizing extra ultraviolet (EUV) flux and the extent to which the ionosphere is open to the radiation determined by the solar zenith angle (SZA); and 2) the precipitation of magnetospheric particles. Magnetospheric particle precipitation strongly depends on the direction of the interplanetary magnetic field (IMF) [*Hardy*, 1985; *Hardy et al.*, 1987; *Fuller-Rowell and Evans*, 1987; *Newell et al.*, 2009, 2010], described by the angle of the magnetic field vector in the plane of the Earth's magnetic field perpendicular to the Sun, or the clock angle. Therefore, the SZA and IMF clock angle are two of the strongest controlling parameters for the distribution of FACs. Much work with numerous data sets has led to a stronger understanding of the FAC dependencies on SZA [*Neubert and Christiansen*, 2003; *Ohtani et al.*, 2005; *Wang et al.*, 2005; *Coxon et al.*, 2016, and references therein] and IMF clock angle [*Weimer*, 2001; *Juusola et al.*, 2009; *Wing et al.*, 2010; *Korth et al.*, 2014; *Milan et al.*, 2015; *Carter et al.*, 2016, and references therein]. Recently, the advent of the Active Magnetosphere and Planetary Electrodynamics Response Experiment (AMPERE) [*An-*

derson et al., 2000; *Waters et al.*, 2001; *Anderson et al.*, 2008] created the opportunity to study the large-scale FACs (3° magnetic latitude resolution) at high cadence (10-minutes) and is contributing to improved definition of the characteristics of large-scale FACs and their dependence on controlling parameters.

However, although large-scale FAC understanding and specification have been improved, smaller scale FACs are not well understood. In recent years, improved high-resolution modeling and new observations have called into question whether large-scale FACs are sufficient to describe magnetosphere-ionosphere (MI) coupling and what role and impact smaller scales have on the entire geospace system. Theory [*Streltsov and Lotko*, 2004] and statistical and case study results [*Sugiura et al.*, 1982; *Lühr et al.*, 1994; *Hasunuma et al.*, 2008; *Zou et al.*, 2016] each indicate the potential significant influence of FAC structuring at scales below the global R1/R2 scale depicted by *Iijima and Potemra* [1978]. Further, significant differences in the characteristics of FACs at different scales have been found [*Neubert and Christiansen*, 2003; *Gjerloev et al.*, 2011; *Lühr et al.*, 2015]. The understanding of FACs across multiple scales is complicated by strong magnetic latitude (MLAT) and magnetic local time (MLT) dependencies [*Weimer*, 2001; *Juusola et al.*, 2009; *Clausen et al.*, 2012; *Juusola et al.*, 2014], which are additionally modified by various controlling parameters, including the SZA [*Cattell et al.*, 2003; *Ohtani et al.*, 2005; *Wang et al.*, 2005] and IMF clock angle [*Korth et al.*, 2010; *Carter et al.*, 2016]. Despite recognition of their importance, there is a lack of understanding of FACs at scales below ∼100s kilometers. We address this lack of understanding by studying the characteristics, controlling parameters, and ionosphere-thermosphere (IT) impact of multi-scale FACs - from small-scales (∼10-150 km, <1° latitudinal width) to mesoscales (∼150-250 km, 1-2° latitudinal width)

to large-scales (>250 km)). Note that we refer to FAC scales under 10 km as Alfvénic [*Chaston et al.*, 2003; *Le et al.*, 2009] and such scales are not the subject of this manuscript.

We are now in a position to gain new knowledge about multi-scale FACs because of the availability of reliable estimates across a range of scales. The European Space Agency Swarm mission provides FAC estimates across scales, and AMPERE data provide complementary large-scale information. Together, Swarm and AMPERE produce a powerful database with which to study multi-scale FACs.

To investigate multi-scale FACs, we emphasize the terms repeatability and characteristics to describe behavior at different scales. In short, if a system is repeatable then the same behavior will be observed for a given input, and that behavior is then defined as a characteristic. There has been strong recent evidence that FACs represent repeatable behavior for the exchange of energy and momentum between the magnetosphere and ionosphere [*Gjerloev et al.*, 2011; *Lühr et al.*, 2015; *Humberset et al.*, 2017]. However, no comprehensive investigation of FAC characteristics across different scale sizes has been conducted. We address this lack of critical information for the MIT system by investigating characteristics of FACs from small-scales to large-scales using Swarm and AMPERE data, and attempt to quantify the characteristics of the *departure* of small-scales and mesoscales from large-scale FAC behavior. Further, it is well understood that the characteristics of the MIT system change based on the input (i.e., solar wind forcing). We, therefore, also investigate multi-scale FAC characteristics as a function of the controlling parameters of the MIT system, focusing on the IMF orientation as the dominant factor controlling the distribution of FACs [*Weimer*, 2001].

Therefore, our study is motivated by three critical questions:

- Are the characteristics of FACs the same across scales?
- Do small- and mesoscale FACs exhibit similar dependencies on solar wind and geomagnetic activity parameters as large-scales?
- To what extent do observed FACs depart from the large-scale picture typically used to model the currents, and does this departure depend on the scale size?

In this paper, we make progress toward answering each of these questions and present a discussion of the impact of our findings on the MIT system. We provide a summary table in Section 5.3 as a quick reference for our findings regarding the differences between multi-scale FACs.

This paper is organized in the following way: First, we describe the data and methods in Sections 2 and 3, respectively. We present the results in Section 4, including the characteristics of FACs at multiple scales, dependencies of FACs across scales on various controlling parameters, focusing primarily on IMF orientation, and multi-scale degree of departure, a novel method to quantify the difference between small- and mesoscale FACs with respect to large-scale statistical R1/R2 FACs. We address the significance of our results in Section 5, providing a discussion of the results with particular focus on the impact of the demonstrated multi-scale FACs on the IT system. We close in Sections 5.4 and 6 with thoughts on the future implications of this work and concluding remarks.

2. Data

The objective of this paper is to study the characteristics, controlling parameters, and relationships of multi-scale FACs, which requires FAC data across a range of scales. We take advantage of the European Space Agency (ESA) Swarm mission to provide small-scale

(∼10-150 km, <1° latitudinal width), mesoscale (∼150-250 km, 1-2° latitudinal width), and large-scale (>250 km, >∼2° latitudinal width) data, and the AMPERE mission to provide complementary large-scale FAC data. Altitude Adjusted Corrected Geomagnetic (AACGM) coordinates [*Shepherd*, 2014] are used for all data.

2.1. Swarm

Swarm is the fifth Earth Explorer mission in the ESA Living Planet Programme and consists of three closely spaced satellites, designated A, B, and C. Swarms A and C orbit side by side at 460 km altitude, separated by 1.4° in longitude, while Swarm B orbits slightly higher at 520 km. Swarms A and C are at an orbital inclination of 87.5°, and that of Swarm B is slightly higher, creating a 20° increase in the angle between the orbital planes per year. The satellites were launched on November 22, 2013 and achieved final constellation configuration in mid-April 2014.

The Swarm science team uses the vector fluxgate magnetometer measurements onboard each spacecraft to routinely produce estimates of the FAC density, using Ampère's law and a model of the geomagnetic and magnetospheric magnetic fields [*Ritter et al.*, 2013; *Lühr et al.*, 2015]. FAC estimates are produced for each spacecraft (i.e., single-satellite estimates) and provided by the science team as level 2 data products (https://earth.esa.int/web/guest/swarm/data-access) [*Olsen et al.*, 2013; *Stolle et al.*, 2017; *Swarm Level 2 Processing System Consortium*, 2012]. The geometry of the Swarm constellation provides the opportunity to also estimate FACs with a dual-satellite approach. The dual-satellite estimate uses consecutive magnetometer measurements from Swarms A and C, located at a common altitude and separated by roughly 1.4° in longi-

tude, corresponding to ∼50 km at 70° MLAT, to define a quad of four data points from which the integral form of Ampère's Law can be evaluated [*Ritter et al.*, 2013].

We analyze Swarm data for the two year period spanning 2015-2016, including single-satellite estimates from Swarm A and dual-satellite estimates from Swarms A and C (Swarm AC).

2.2. AMPERE

The Active Magnetosphere and Planetary Electrodynamics Response Experiment (AMPERE) [*Anderson et al.*, 2000] collects magnetic perturbation data from engineering grade magnetometers aboard 66 spacecraft in the Iridium commercial communication constellation (eleven satellites in six different orbital planes), each with an orbital period of 104 min and altitude of 780 km. The cross-track magnetic perturbations are processed with a least squares spherical harmonic fit to produce global distributions of radial current densities [*Waters et al.*, 2001; *Anderson et al.*, 2008, 2014]. Radial refers to currents directed toward or away from the surface of the Earth. Therefore, at MLATs >60° the radial currents largely correspond to FACs. AMPERE FACs are estimated with 3° MLAT resolution, though the resultant spherical harmonic functions can be evaluated at any location and are provided by the AMPERE science team (http://ampere.jhuapl.edu/) on a 1° MLAT × 1 hour MLT grid. AMPERE FAC estimates, therefore, roughly yield resolutions of 350 km scale size. Observations accumulated over a 10 min window are included for each fit, and fits are computed at a 2 min cadence (i.e., consecutive fits contain overlapping data). AMPERE FACs with magnitude less than 0.05 μA m^{-2} are excluded from analysis. Note that this threshold is lower than previous work (0.2 [*Clausen et al.*, 2012], 0.16 [*Anderson*

et al., 2014], and 0.1 [*Carter et al.*, 2016]), but we apply additional, rigorous constraints to the data, detailed in Section 3, such that a slightly lower initial threshold is justified.

To compare Swarm and AMPERE observations with a nominal large-scale FAC distribution we use the fitting method of *Clausen et al.* [2012] (C2012), which determines the MLAT and strength of the R1/R2 FACs along each local time meridian separately. Full details of the use of this method in this paper are provided in Section 3.5.

2.3. Solar wind data

We use 5 min resolution solar wind data from NASA's Coordinated Data Analysis Web (CDAWeb-https://cdaweb.sci.gsfc.nasa.gov/). These data contain measurements from multiple spacecraft, accounting for estimated spacecraft-to-magnetopause propagation times. We apply an additional 15 min delay to take into account the signal transit time from the magnetopause to low Earth orbital altitudes [*Vennerstrøm et al.*, 2002; *Neubert and Christiansen*, 2003; *Juusola et al.*, 2009].

3. Methodology

3.1. FAC scale sizes

Using Swarm A single-satellite, Swarm AC dual-satellite, and AMPERE data simultaneously allows us to study FACs across multiple scales and to understand their characteristics and relationships.

Swarm A single-satellite estimates are narrow band-pass (Hanning) filtered [*Gjerloev et al.*, 2011; *Lühr et al.*, 2015; *Forsyth et al.*, 2017] with various cutoff frequencies to remove small-scale variations and synthesize larger scale FACs. Taking the common assumption that the currents through which the spacecraft are traveling are temporally and spatially

stationary (this rather critical assumption is discussed further in Section 3.2), different filtering periods directly correspond to different spatial scales and allow us to examine the properties of different FAC spatial scales. Because the Swarm satellites move in the polar direction, the scale sizes correspond to the MLAT direction. Assuming the satellites travel perpendicularly to the vertically aligned current sheets, a good assumption for the Swarm polar orbit [*Lühr et al.*, 2015], spatial scales are calculated by multiplying the filter period by the spacecraft velocity [*Forsyth et al.*, 2017]. The smallest scale that can be resolved by the Swarm satellite (i.e., with no filter applied) is ∼7.5 km given by the 1 Hz cadence of magnetometer measurements and the ∼7.5 km/s spacecraft velocity. However, *Forsyth et al.* [2017] found that the 7.5 km scale size FAC estimates often violate the necessary single-satellite FAC estimation assumptions, and we, therefore, do not compute statistical results from these scales in this manuscript. The magnetic data used for the Swarm level 2 dual-satellite FAC calculation is low-pass filtered with a cut-off frequency of 20 seconds, and, therefore, can only resolve scale sizes greater than 150 km (20 sec × 7.5 km/sec = 150 km) [*Olsen et al.*, 2013; *Stolle et al.*, 2017].

Finally, AMPERE spherical harmonic fits are computed with a latitudinal resolution of 3° and data products are provided with the fits evaluated on a 1° MLAT × 1 hour MLT grid. Therefore, the AMPERE FAC estimates roughly yield 350 km scale size.

Table 1 details the scale sizes examined in this work. We choose filter cutoff periods to study Swarm A FAC estimates across small (∼50 km), meso (∼150 km), and large-scales (∼350 km). These choices were additionally influenced by the desire to compare different estimates of mesoscale (Swarm A single-satellite and Swarm AC dual-satellite) and large-scale (Swarm A single-satellite and AMPERE) FACs. Together, Swarm single-

and dual-satellite and AMPERE FAC estimates provide an ideal combination of small-scale, mesoscale, and large-scale information. We note that in this paper we examine FACs resolved to small scale and those that are smoothed to larger scales, such that 'large scale' refers to spatial smoothing.

3.2. Swarm single-satellite quality control

Swarm single-satellite estimates are subject to the following important assumptions:

1. stationary currents (i.e., the current density profile does not change during the time it takes the spacecraft to cross them)

2. static currents (i.e., the currents do not move in space during successive satellite measurements)

3. perpendicular, infinite currents (i.e., the satellite encounters the current at a 90° angle)

The static assumption is valid when the motion of the satellite crossing the FAC feature is much greater than the movement of the feature itself (i.e., to convert from temporal variations to spatial scales, the velocity of the spacecraft with respect to the FAC feature must be large [*Lühr et al.*, 1994]). Given the high spacecraft velocities of low Earth orbit satellite, this is generally true for mesoscale and large-scale FACs. However, the static assumption may break down for small-scale FACs, which generally exhibit more rapid variations [*Lühr et al.*, 1994; *Le et al.*, 2009; *Gjerloev et al.*, 2011]. Additionally, with decreasing scale size the infinite current sheet assumption becomes less robust. We address these complications through application of the correlation and amplitude filters developed by *Forsyth et al.* [2017] to robustly remove single-satellite FAC data that violate the stationary and static assumptions. Note that we also examine Swarm dual-satellite FAC

estimates from the combination of Swarm A and C magnetic perturbation observations, which can be estimated more uniquely and directly [*Ritter et al.*, 2013].

Forsyth et al. [2017] developed a method to identify when single-satellite Swarm FAC estimates are unreliable based on two quantities, both computed using FAC estimates from Swarms A and C, that collectively determine if the FACs observed by Swarms A and C are similar: 1) the linear correlation (to determine if the form of the FACs observed by both satellites is similar); and 2) the gradient of the least squares fit of the FAC amplitudes (to determine if the magnitude of the FACs observed by both satellites is similar). The inclusion of the latter measure represents a new level of rigor with which to evaluate the validity of single-satellite estimates. Together, these measures determine when observed FACs are the same between both satellite estimates, and, therefore, the satellites are encountering stationary currents in the normal direction (i.e., when the single-satellite assumptions are valid). If the Swarm A and C FAC estimates are identical, then the correlation and gradient of the least squares fit would both be unity. This will never be the case in practice, owing to observation and calculation uncertainties, so we choose filter thresholds of 0.5 for the correlation and 0.5-1.5 for the amplitude fit gradient to define valid single-satellite estimates. *Forsyth et al.* [2017] presented results for more conservative filter thresholds. However, our reduced thresholds are justified by the fact that the size of the Hanning filter window has a larger effect on the validity of the assumptions than the filter values (larger windows produce more reliable FACs) [*C. Forsyth, personal communication* 2017] and that we exclude the unfiltered FAC data (the smallest scales at 7.5 km) from our analyses. Effectively, this means that we start from a more reliable baseline for all single-satellite FAC estimates. We have computed the correlation and linear fit parameters

from Swarm A and C FAC estimates that have been band-pass filtered using a cut-off frequency of 13 sec, such that, appropriately, small-scale FACs ($\sim$100 km scale size) are used to determine the validity of the single-satellite data. Parameter values are computed for every data point in the entire database. Roughly 35% of the data over the analysis period meet these requirements, and are used for our analyses.

In addition to these robust filters, the Swarm single- and dual-satellite Level 2 FAC data products also each contain quality flags to identify numerous conditions under which the FAC estimates are unreliable, such as data points when the magnetic field inclination angle is greater than $|30°|$ (i.e., roughly $\pm 15°$ around the magnetic equator), no magnetospheric field model coefficient data exist, and, for the dual-satellite estimate, when the horizontal spacecraft separation is too small (3 km is chosen and corresponds to geographic latitudes $>86°$ [*Stolle et al.*, 2017]). We reject all FAC data for which a quality flag indicating questionable or bad data exists. Single-satellite data are removed for points at geographic latitudes $>86°$ to correspond to the dual-satellite data. For full details of the data quality flags see *Stolle et al.* [2017] or the Swarm Detailed Processing Model Document [*Swarm Level 2 Processing System Consortium*, 2012].

3.3. FAC data accumulation and pass-by-pass analysis

We compare Swarm single- and dual-satellite and AMPERE FACs for data accumulated over two full years from 2015 to 2016. Given that Swarm A and C precess 12 hours in MLT over 133 days [*Stolle et al.*, 2013], our database provides roughly 5.5-fold coverage of all MLTs. Data are analyzed on a pass-by-pass basis, where a pass is defined as a leg of the Swarm A orbit between 50° and the maximum MLAT, such that two 'passes' occur for each Swarm A hemispheric crossing. AMPERE data are sampled along the Swarm

A orbit. Because AMPERE data are less reliable in the southern hemisphere [*Anderson et al.*, 2017], in this paper we analyze data from the northern hemisphere only.

Figure 2 and the following steps summarize our analyses for each Swarm pass. We choose data from February 23, 2015 (04:41-04:52 UT) to illustrate a representative Swarm pass.

1. Swarm FAC data are selected for the given pass (defined between 50° and maximum MLAT, Figure 2a);

2. Our rigorous quality control process rejects data where Swarm FAC information is not robust, excluding data that do not meet single-satellite FAC assumptions (Figure 2b) and those that are flagged in Swarm data processing (see Section 3.2 above);

3. AMPERE FAC data are sampled along the Swarm satellite track (Figures 2a and c);

4. R1/R2 FAC fits to AMPERE data for each MLT using the fitting method of *Clausen et al.* [2012] (hereafter C2012) are calculated for each MLT and sampled along the Swarm satellite track (Figures 2a and d, see Section 3.5 below)

5. Linear correlations are calculated between Swarm and AMPERE FAC densities that exceed a 0.1 μA m^{-2} threshold [*Carter et al.*, 2016] (Figure 2e);

6. Degree of departure measures, introduced in Section 3.5 below, are calculated between Swarm and AMPERE and C2012 (Figure 2f);

7. Each data point is saved along with key summary data (e.g., average MLAT and MLT, peak upward and downward FACs and their MLAT-MLT locations, pass-summed FACs, median lagged solar wind data, etc.). Summary data are described in further detail with respect to the corresponding result in Section 4 below.

Figure 2a shows FAC data for a representative Swarm pass on February 23, 2015 between 04:41-04:52 UT. FAC densities are shown for Swarm A at three scales (small, meso, and large), Swarm AC, AMPERE, and C2012. The x-axis provides the MLT, MLAT, and UT information for the Swarm A satellite, which is used to geolocate all data. Thin color-coordinated vertical bars indicate the locations of maximum and minimum FACs for each scale size. Note that because the 7.5 km scale size data rarely meet the single-satellite FAC estimation assumptions (Section 3.2) they are not analyzed further below, but are presented here to give a complete picture of the data.

Figure 2b details the single-satellite FAC quality control procedure created by *Forsyth et al.* [2017] and discussed in Section 3.2. Swarm A unfiltered (i.e., 1 Hz) FAC densities are shown in the top panel. The middle and bottom panels show the correlation coefficients and linear fit gradients calculated for each data point using the 13 sec frequency filter window, respectively. Horizontal black lines on each plot indicate our selected thresholds and data meeting the single-spacecraft FAC estimation assumptions are indicated by vertical green bars in the top panel.

Figures 2c and d show the polar distributions of AMPERE and C2012 FACs, respectively, for the time period of the Swarm pass. In each polar plot AACGM MLAT-MLT distributions are shown with local noon to the top and dawn to the right. The plots extend to 50° MLAT and dashed rings are provided at 10° increments. The Swarm satellite track is superimposed on both figures. Red indicates upward FACs (flowing away from the ionosphere) and blue indicates downward FACs (flowing toward the ionosphere). This convention is used throughout the manuscript. Local time meridians where no data are

plotted in Figure 3.2d indicate areas where the C2012 fit was rejected (see Section 3.5 below for rejection criteria).

We analyze the characteristics of these data in two separate ways: 1) compute statistics from all data points over the entire time period, independent of the pass; and 2) summarize the key information of each pass and compare these data between scales. We specifically identify which analysis method is used to produce individual results in Section 4.

3.4. Correlation analysis of FACs

We compute correlations between Swarm and AMPERE FAC data for each Swarm pass. Figure 2(e) shows the linear correlation coefficients for the February 23, 2015 Swarm pass between 04:41-04:52 UT. Data point sizes and location on the y-axis reflect the magnitude of the correlation. We only correlate data exceeding a 0.1 μA m^{-2} threshold [*Carter et al.*, 2016] to ensure that only stronger FAC signals contribute to the correlations. Further, any correlations that do not meet a 95% significance level are rejected (i.e., if the significance level for testing the hypothesis that no relationship exists between the data is less than 0.05, then the correlation is deemed significant). Correlations between Swarm and AMPERE are analyzed as a function of MLT and interplanetary magnetic field (IMF) orientation (Section 4.2.2), such that we obtain $C(\text{MLT}, \text{IMF orientation}, \text{scale size})$ for each pass. Correlating different scale FACs over the same time interval, and determining the correlation characteristics as a function of MLT/IMF orientation is a novel approach, similar to, but distinct from, correlation analyses of FAC data conducted by *Gjerloev et al.* [2011] and *Lühr et al.* [2015]. To our knowledge, this is the first time such analysis has been conducted.

3.5. The nominal FAC distribution and degree of departure

Our analyses produce a rich database through which to study the characteristics and controlling parameters of multi-scale FACs. However, it is also critical to understand the relationships between the FAC scale sizes themselves. To quantitatively study multi-scale FAC relationships we rely on the concept of 'anomalous' behavior. The definition of anomalous behavior in geospace is a difficult problem with many possible solutions [*Wang et al.*, 2016]. We solve this issue by noting that the ability to define anomalous behavior requires three components: 1) a background or nominal state; 2) a disturbed or alternate state; and 3) quantification of the difference between the two. In this paper we will use the term 'degree of departure' to describe the quantification of anomalous FAC behavior. Understanding degree of departure is critical to new knowledge about the significance of multi-scale FACs, and such a comparison has never before been performed in a comprehensive statistical manner.

To define degree of departure we must first establish the nominal FAC distribution. We attempt to quantify the importance of multi-scale FACs with respect to their difference from the current large-scale understanding, and, therefore, choose large-scale FACs as the baseline (i.e., the R1/R2 system). To define these FACs we use the fitting method developed by *Clausen et al.* [2012] to derive R1/R2 FACs from AMPERE data and subsequently used prolifically to study the characteristics of large-scale FACs [*Coxon et al.*, 2014a, b; *Milan et al.*, 2015; *Coxon et al.*, 2016; *Carter et al.*, 2016]. We believe the R1/R2 FACs produced from the *Clausen et al.* [2012] method (hereafter C2012) more faithfully represent the distributions than empirical approaches such as [*Weimer*, 2001, 2005] because they are driven by instantaneous observations (shortcomings of the *Weimer* [2005]

empirical model for dynamic representation during a geomagnetic storm are discussed in *Huang et al.* [2014]). We, therefore, interpret this method as the best available data-driven instantaneous fit to large-scale FACs for our purposes. A strong advantage of this choice is that it allows us to control for instances where the fits are unreliable and avoid drawing conclusions from distributions that are not supported by the data. Other viable approaches could, of course, be used. However, given that the geospace modeling commonly relies on global FAC specification, and specifically on the C2012 method, ours is an appropriate and pragmatic approach. To compare C2012 FACs with Swarm and AMPERE observations, we perform the following steps:

1. Derive C2012 FACs at each hour of MLT from the AMPERE data at the median time of a given Swarm A pass, producing 24 separate MLAT profiles of FACs;

2. For each MLT discard unreliable fits based on criteria developed in *Clausen et al.* [2012] and *Carter et al.* [2016] (i.e., if R1/R2 system is located too close to the pole, the width of the system is too narrow, or if the polarity of the system is reversed from the expected R1/R2 sense);

3. Sample the C2012 FACs along the Swarm A orbit, in the same manner that AMPERE observations are sampled;

4. Compute differences between Swarm A, Swarm AC, and AMPERE FACs and C2012 FACs. These differences constitute the 'degree of departure.'

The characteristics of the success of the C2012 FAC fitting method have been discussed in detail in *Clausen et al.* [2012] and *Carter et al.* [2016] and are very similar in this work. Briefly, we find a high rate of success at dusk and dawn MLT sectors and increased success for increased AMPERE current density. The method fails more often in the

midnight and noon MLT sectors and is, in general, unsuccessful in situations where more than two current sheets exist prominently, during periods where Region 0 (polar cap) [*Kustov et al.*, 2000; *Wing et al.*, 2010] currents are present, for instance.

C2012 FACs for the sample pass are shown in Figure 2d. The minimum scale size of these FACs is commensurate with the AMPERE data from which they are derived (i.e., roughly 350 km). MLT sectors for which the C2012 fit was unreliable are rejected. Additionally, degree of departure data are rejected for passes in which the C2012 FACs contain too few data points along the Swarm satellite track to produce statistically significant comparisons. In this manuscript degree of departure always refers to a comparison between the observed FACs (Swarm and AMPERE) and the fitted FACs (C2012).

There are many ways to summarize the degree of departure. We show one example degree of departure metric in Figure 2f: the difference between the pass-summed upward and downward FACs. Differences are computed between the absolute values of Swarm and AMPERE FACs and the C2012 FACs. Differences for the upward and downward FACs are shown in the top and bottom panels of Figure 2f, respectively. Sizes of the data points reflect the size of the departure of the observations from the fit. Positive values signify that the absolute value of the FAC observation is greater than the absolute value of the C2012 fitted FAC and vice versa. In Section 4.4 we explore several metrics to quantify the degree of departure.

3.6. Inherent limitations

Before presenting the results of our analyses, we first detail important points about the limitations of our approach.

• Though we have used a robust algorithm to remove single-satellite FAC data that do not meet assumptions of stationary and static currents, the algorithm inevitably fails to remove all such estimates. However, these instances will be few (supported by extensive orbit-by-orbit investigation) and the statistical results presented below are not sensitive to these limited instances.

• There are numerous ways to define the nominal or background state for the degree of departure analyses. Different choices of the background state will inevitably produce different results, and the choice should be driven by the objectives of the analysis. Because we are attempting to determine differences between multi-scale FACs, we have chosen a data-driven fit to large-scale R1/R2 FACs [*Clausen et al.*, 2012] that has been used prolifically in the FAC literature to study the characteristics of large-scale FACs [*Coxon et al.*, 2014a, b; *Milan et al.*, 2015; *Coxon et al.*, 2016; *Carter et al.*, 2016]. This choice represents perhaps our best ability to model the R1/R2 currents on an instantaneous basis, and, therefore, ideally serves the objectives of this study.

• We have primarily investigated statistical results for multi-scale FACs. Statistically summarizing the data in our full database inevitably reduces the information content of the original data.

• The statistical results presented here allow general conclusions and implications. They do not allow detailed definition of individual case characteristics. The database we have created will be invaluable to future case studies that will incorporate additional data on a variety of variables. Section 5.4 provides a more detailed discussion of future considerations.

4. Results

Our results are organized into two categories: 1) characteristics and controlling parameters and 2) degree of departure. The characteristics and controlling parameters of FACs are examined in Sections 4.1-4.3. These results are based solely on Swarm and AMPERE observations. The degree of departure is then examined in Section 4.4. Therefore, in Section 4.4 we shift to comparisons of Swarm and AMPERE observations with C2012 fitted FACs. All results in Section 4.4 refer to such comparisons.

4.1. Coverage and observational details

For the 2015-2016 period we processed roughly 21900 Swarm passes, which corresponds to ∼63 million data points and ∼16 million over the northern hemisphere poleward of 45° MLAT. These data are analyzed in this manuscript. Taking into account each of the quality control and rejection criteria detailed in Section 3, the database includes ∼18600 passes and nearly 11 million observations. Roughly 35% of these 11 million (or nearly 4 million) observations meet the single-satellite estimation assumptions and are used to produce the results below.

Figures 3 and 4 give an overview of the observational characteristics for our FAC database. Figure 4 shows the number of observations for (a) each MLAT between 55-85° and (b) all MLTs. The distributions are uniform, showing no bias in MLT and a slight decrease in the number of data points poleward of 80° MLAT. There is a peak in the MLAT observation density around 78-80°, which corresponds to the observational coverage reported by *Forsyth et al.* [2017].

Figure 4 shows the occurrences of (a) IMF clock angle orientation, (b) disturbance storm time index (Dst), and (c) auroral electrojet index (AE). A single value of each parameter

is recorded for each Swarm pass. IMF orientation is defined by the clock angle, which is the angle between geocentric solar magnetic (GSM) north and the projection of the IMF vector onto the GSM Y-Z plane:

$$\theta = \tan^{-1}\left(\frac{B_{\mathrm{Y,GSM}}}{B_{\mathrm{Z,GSM}}}\right). \quad (1)$$

The GSM coordinate system is centered at the Earth, with x-axis oriented towards the Sun, z-axis perpendicular to the x-axis and in the plane containing the x-axis and the Earth's geomagnetic pole (positive northward), and y-axis completing the orthogonal set. The y-axis is, therefore, positive towards dusk. We define eight IMF clock angle bins, centered at 0°, 45°, 90°, 135°, 180°, 225°, 270°, and 315° and each spanning 45°. These bins will be used for all IMF clock angle dependent results in this manuscript.

IMF clock angle occurrences are distributed relatively uniformly, with only a slightly reduced number of occurrences of purely northward and southward IMF (0° and 180°, respectively), which is typical [*Fear et al.*, 2012]. The higher number of occurrences of Dst and AE at smaller (absolute) values indicates that the average results shown in this work will be more indicative of periods of reduced activity. The range of the Dst and AE indices over the whole period are −212-60 nT and 7-1901 nT, respectively.

4.2. Characteristics of multi-scale FACs

We first explore the characteristics of multi-scale FACs. Figure 5 shows polar plots of the observation density and average FACs computed using every observation. We use an equal area binning scheme to mitigate the latitudinal variation that affects fixed resolution grids at mid and high latitudes [*Ruohoniemi and Baker*, 1998]. The equal area gridding

scheme uses a constant 1° MLAT resolution and variable MLT resolution (0.28 h at 50° MLAT to ~2.18 h at 85° MLAT), yielding a total of 1749 grid points between 50-90°. We use the sign convention that positive FACs are away from the ionosphere (upward currents) and negative FACs are toward the ionosphere (downward currents). All polar plots shown in this manuscript follow these conventions.

Figure 5a shows the distribution of data counts in the Northern Hemisphere for the 2015-2016 period, including only the quality controlled data (see Section 3.2). The highest density of observations occurs at latitudes poleward of roughly 65°, though good coverage is provided at all MLATs. Our database covers each MLT ~5.5 times such that there are no data gaps for any MLT, and coverage is reasonably uniform in MLT. Figures 5b-f each show two panels: (top) the average FACs and (bottom) the sub-grid level variability. Sub-grid scale variability (or sub-resolution variability) is defined as the variance of all observations in a given MLAT-MLT bin. These results are shown for the various FAC data sets in our database. The scale size increases from left to right such that Figure 5b is the smallest scale studied (50 km) and Figure 5f is the largest (350 km). The average distributions across scales are similar, showing the well-known R1/R2 FAC patterns in the dawn and dusk MLT sectors. At all scales R0 FACs are evident in the high-latitude dayside region, and the change of polarities of the R1/R2 systems is shifted slightly pre-midnight. This could be the result of a slightly larger number of IMF $+B_Y$ occurrences (Figure 4a), which controls the location of dawn-dusk FAC polarity change [*He et al.*, 2012; *Carter et al.*, 2016]. There are a few exceptions to the agreement between scales. Smaller scales yield larger R2 FACs, and these currents are more distinctly defined in latitude (comparing, for instance Figures 5b and f). It should not be surprising that

such close distributions are found across scales for average results. The bin-averaging has the effect of smoothing out the differences that exist between the small- and large-scales. To investigate the extent to which this occurs, the bottom panels in Figures 5b-f display the sub-grid level variability of the average distributions. Significant differences exist between the amount and location of variability observed for each scale. At 50 km scale size (Figure 5b) the most intense variability occurs in the dayside sector between 70-80° MLAT. Enhanced variability is also observed in the midnight sector between 60-70° MLAT and dawn and dusk sectors at MLATs between the R1/R2 FACs shown in the top panel. These patterns of variability disappear with increasing scale size, and at 350 km (Figures 5e and f) there is virtually no variability observed in either the Swarm or AMPERE data. Clearly the small scale-scale behavior is consistent with, but contains significant departure from, the large-scale behavior.

4.2.1. Peak FACs

Next we examine the peak FACs, and their MLAT-MLT location, as a function of scale size. For each pass, we calculated and recorded the peak FAC densities (separately for upward and downward directions) along with their MLAT location. The MLT location of the peak FACs is given by the median MLT for each pass. We then calculated the average values over all passes (averages for both the peak FAC densities and their MLAT location) and binned them using 1 h MLT bins. These average peak FACs are shown in Figure 6 for each scale size: (a) 50 km; (b) 150 km; (c); Swarm AC; (d) 350 km; and (e) AMPERE.

The largest MLAT separation between the upward and downward peak FACs occurs in the dawn and dusk MLT sectors, reaching their maximum separation in the hours

just before 0600 MLT and just after 1800 MLT. In general, the dayside peak FACs are significantly less separated in MLAT, where our results show the positive and negative peaks are nearly collocated. Figure 7a is provided to illustrate the quantitative differences of the MLAT locations at all MLTs, in which we plot $\mathrm{MLAT}_{\text{peak }+J_r} - \mathrm{MLAT}_{\text{peak }-J_r}$. Swarm A 350 km scale size gives the greatest separation of peak FACs throughout the dawn and dusk sectors, generally around 3-4°, while AMPERE and Swarm AC peak FACs are least separated in these sectors. The polarity reverseal in the pre-midnight (∼2300 MLT) region is remarkably well captured by the Swarm data, whereas variability between adjacent MLT bins on the nightside in AMPERE (see, for instance, the sharp jump in MLAT location between 2300-0100-0200 MLT in Figure 6e) suggests difficulty of the large-scale AMPERE spherical harmonic fit to appropriately identify FACs in this region. AMPERE results also show peak FACs at more poleward latitudes than the Swarm data at all local times except near noon, where Swarm and AMPERE both observe peak values near 78° MLAT.

Current continuity requires that FACs close horizontally through the ionosphere and differences in MLAT separation of peak FACs between scales and as a function of MLT has important implications for current closure in the IT system. In the case that closure currents generally occur between the peak FACs, larger separation would indicate closure currents over larger areas. This is likely the case at the dawn and dusk sectors where R1/R2 FACs commonly close between one another [*Hruška*, 1981] and imbalances largely close over the polar cap [*Le et al.*, 2010]. On the dayside the separation between peaks is smaller, potentially resulting in localized current closure. The reduced dayside separation is different from the results reported by *Wang et al.* [2005] using CHAMP satellite data

for the southern hemisphere (their Figure 7), which may indicate a potential hemispheric asymmetry at dayside MLTs.

The orange and green arrows superimposed on Figures 6 and 7 point out the 0500 and 1700 local times, respectively. These locations are illustrative of the fact that relationships among scales are not necessarily intuitive at all local times. At 0500 the Swarm AC and Swarm A 50 km scale observations indicate that the peak densities are separated by $<2^{\circ}$ MLAT, while all other observations indicate a separation of $>2^{\circ}$. However, at 1700 MLT, AMPERE yields the smallest separation and Swarm AC and Swarm A 50 km scale are no longer equal. Though differences are modest due to averaging, the results illustrate that multi-scale FAC relationships are complicated in terms of local time dependence, and the large-scale local time dependence cannot be assumed to be accurate for smaller scales. More generally, the MLAT-MLT characteristics of the peak FACs do not appear to depend on scale size in a simple way. Case studies will augment the statistical results shown in Figures 6-7 and help explain specific relationships, such as the reason for the reduced separation in the Swarm AC and AMPERE FAC estimates in the dawn and dusk LT sectors with respect to Swarm A results on comparable scales.

Note that Figure 7a did not compare between scales (i.e., Swarm A 350 km data were only compared with themselves, and not, for instance, with AMPERE data) and differences in MLAT location are plotted [deg]. Alternatively, Figures 7b and c highlight the differences between the peak densities [μA m^{-2}] across scales, using AMPERE as a baseline. We show the difference between Swarm and AMPERE upward (Figure 7b) and downward (Figure 7c) peak FACs (i.e.,peak $\pm J_{r,\ \mathrm{Swarm}}$ − peak $\pm J_{r,\ \mathrm{AMPERE}}$). Absolute values are used for the negative FACs. Different scales are indicated by shades of red

(upward FACs) and blue (downward FACs) to remain consistent with the sign-color convention used in this paper. AMPERE and Swarm 350 km scales are in close agreement. Disagreement increases with decreasing scale size, and average values of 1.5-2.5 μA m^{-2} characterize the difference between 50 km and 350 km scale sizes. These differences are comparable to average magnitudes of large-scale FAC densities [*Clausen et al.*, 2012] and are quite significant. Differences are maximized at noon and 0900 MLT for the positive and negative directions, respectively. Dawn-dusk asymmetries are clearly present, and are more pronounced for negative peak densities. We reiterate that instantaneous differences can depart from the average patterns shown in Figures 6 and 7 significantly.

4.2.2. Multi-scale FAC correlations

Correlating FACs at different scales is one metric to determine whether the *form* of FACs varies across scale. We examine Swarm-AMPERE correlations in Figure 8 as a function of MLT and IMF clock angle (Equation 1). The IMF clock angle for a given pass is defined as the median of the values at the beginning, middle, and end times of the pass, each lagged by 15 minutes to account for signal transit time from the magnetopause to the Swarm/AMERE orbital altitudes [*Vennerstrøm et al.*, 2002; *Neubert and Christiansen*, 2003; *Juusola et al.*, 2009].

In Figure 8 each panel represents a set of average linear correlations for a different Swarm-AMPERE comparison: Swarm A 50 km scale-AMPERE (Figure 8a), Swarm A 150 km scale-AMPERE (Figure 8b), Swarm AC 150 km scale-AMPERE (Figure 8c), and Swarm A 350 km scale-AMPERE (Figure 8d). For each Swarm pass, one correlation coefficient is calculated and tagged with the MLT location and 15 min lagged IMF clock angle. Average correlation coefficients are calculated as a function of MLT (x-axis)-IMF

clock angle (y-axis), using bins of 1 hr MLT-45° IMF clock angle. These correlations provide information about the extent to which different scale FACs, represented by Swarm data, have the same form as the large-scale FACs, represented by AMPERE. The x- and y-axes labels give the centers of the MLT-IMF clock angle bins, respectively. Only average correlations greater than 0.4 are plotted.

Given the average nature of the correlations in Figure 8, relationships are, to a certain extent, smeared. However, important relationships emerge. It is immediately clear that correlations between Swarm and AMPERE measurements decrease with decreasing Swarm scale size (correlations in Figure 8a are, in general, smaller than those in Figure 8d) and there are fewer bins where correlations exceed 0.4. The second most apparent feature of Figure 8 is that the largest correlations at all scale sizes exist in the dusk and dawn MLT sectors. When the IMF orientation has a southward component (135, 180, and 225° bins) the small-, meso-, and large-scales have the same form (correlation coefficients $\geq$0.5) in the 0300-0900 (dawn) and 1400-2100 (dusk) MLT sectors. This might be expected given the increased dominance of the large-scale 'background' R1/R2 FAC patterns when southward IMF drives increased FAC densities [*Carter et al.*, 2016]. Increased correlations for these conditions suggests a reduced capability of small scales to change the form of the large-scale pattern, on average. This effect can also be seen for different B_Y directions. Considering the Swarm A 150 km - AMPERE correlations in Figure 8b, the strongest correlations for purely southward IMF (outlined in green) are centered at 1800 MLT. However, as B_Y turns negative (moving downward in the figure to the 270 and 315° bins, highlighted in blue), the region of strongest correlation shifts toward the dayside. When B_Y is negative the upward R1 currents from dusk are more dominant in the

noon sector between 70-80° [*Weimer*, 2005; *Carter et al.*, 2016] and we correspondingly observe greater similarity (e.g., larger correlations) in the smaller and larger scales there. The opposite is true for $+B_Y$, which is reflected in the correlations in the prenoon sector, albeit in a reduced manner (see in Figure 8 the shift in largest correlations from an 0600 MLT center during $-B_Z$ to more dayside MLTs as $+B_Y$ becomes more dominant in the 90 and 45° IMF bins - this effect is most apparent in Figures 8b and c). Northward IMF conditions produce the weakest correlations between scales. This may suggest a relative increase in the influence of small and mesoscale FACs during such conditions.

Finally, correlation coefficients near noon MLT are consistently low across all scales, however there is a scale size dependence. The width of the region of low correlation broadens toward both dawn and dusk with decreasing scale. To illustrate this point, we include dark green bars at the top of Figures 8a, b, and d (correlations between Swarm A and AMPERE data) that span the width of the region on each figure where no correlation exceeding 0.4 exists for the noon MLT sector and purely southward IMF. There is no gap for the Swarm A 350 km - AMPERE correlations (Figure 8d), and the gap is four hours for Swarm A 150 km - AMPERE (Figure 8b) and five hours for Swarm A 50 km - AMPERE (Figure 8a).

In general, we find that similar forms exist across FAC scales for active geomagnetic conditions in the dawn and dusk MLT sectors, but that the forms are less similar in the midnight sector and are significantly different in the noon sector. This suggests that, in an averaged sense, in the dawn and dusk sectors large-scale structure dominates and the small scales do not significantly alter the form, but away from these sectors the smaller scales exist as distinct current systems.

4.3. Controlling parameters of multi-scale FACs

We next examine the controlling parameters of Swarm and AMPERE FACs, particularly focusing on the IMF clock angle.

4.3.1. Interplanetary magnetic field (IMF) clock angle dependence

Each of the figures in this subsection contains polar plots of average FAC densities for eight 45° IMF clock angle bins, defined above. Figure 9 provides the observational density as a function of IMF clock angle. We use the same conventions here that were used for the total observational density shown in Figure 5a. Blue values to the bottom left of each plot are the total number of observations for each IMF orientation. A slightly larger number of observations exist around 78-80°, similar to that observed in Figure 4a. The observations are evenly distributed in MLT and relatively evenly distributed across all clock angles, though the slightly greater number of observations for positive $B_{\mathbf{Y}}$ orientations can be seen and is also shown in Figure 4a.

We first examine the large-scale FACs and compare the Swarm A and AMPERE representations. Figure 10 shows the Swarm A (Figure 10a) 350 km scale size and AMPERE (Figure 10b) FACs. On each of the figures in this section all data are binned onto an equal area MLAT-MLT grid in AACGM coordinates and bin averages are shown. The MLAT resolution is 1°, and the MLT resolution is variable to yield equal area bins (0.28 hours at 50° MLAT to 2.18 hours at 85°). The data plotted are FAC density [μA m^{-2}]. The low-latitude limit on each polar plot is 50°. Noon MLT is at the top of each polar plot with dawn to the right. Clock angles increase in 45° increments in the clockwise direction. To emphasize the strong patterns, bins in which the average FAC density is strictly less than 0.1 μA m^{-2} are left empty.

AMPERE FACs are consistent with previous findings of IMF clock angle dependent large-scale FACs [*Weimer*, 2001; *Korth et al.*, 2010; *Carter et al.*, 2016]. There are several prominent features. During northward IMF (top row, Figure 10b) the most intense FACs are located in the noon sector poleward of distributions for other IMF directions (Region 0 (R0) FACs driven by magnetospheric lobe reconnection [*Carter et al.*, 2016], also called NBZ currents). The NBZ current system for purely northward IMF (top row, middle) [*Saflekos and Potemra*, 1980; *McDiarmid et al.*, 1980] is particularly pronounced. With increasingly southward IMF (moving from top to bottom in Figure 10b), FAC magnitudes increase and R1/R2 FACs become more pronounced while the R0 FACs diminish, consistent with the expanding contracting polar cap paradigm [*Coxon et al.*, 2014a]. IMF $B_{\mathbf{Y}}$ effects are also clearly seen. Looking at the far right column of Figure 10b ($+B_{\mathbf{Y}}$ conditions), the downward R1 currents (blue) appear to extend from dawn through dayside MLTs and feed into the downward R2 currents in the dusk MLT sector. This pattern is clearer for southward IMF conditions. This has been previously reported [*He et al.*, 2012, and references therein]. However, upward R1 currents from the duskside MLT sector connect to high-latitude dayside currents for $+B_{\mathbf{Y}}$ conditions. Opposite relationships hold for $-B_{\mathbf{Y}}$ (left column of Figure 10b).

Figure 10a shows the Swarm A data at roughly the same 350 km scale size resolved by AMPERE. Swarm reflects the prominent features mentioned above and exhibits a large degree of agreement with the AMPERE data. However, two differences are notable: 1) Swarm observes stronger and more distinct R2 FACs; and 2) in general, locations and magnitudes of peak FACs as observed by Swarm and AMPERE are not in complete agreement (we addressed these differences independent of IMF orientation in Section

4.2.1). Differences between Swarm and AMPERE appear to be largest during northward B_Z conditions.

Generally, Figure 10 illustrates agreement among Swarm and AMPERE large-scale FACs and both are consistent with previous FAC morphologies, giving credence to the methodology. We can now investigate the dependence on IMF orientation at smaller scales with confidence. Figure 11 compares FAC distributions at 150 km scale size. Figures 11a and b show the Swarm A (single-satellite) and Swarm AC (dual-satellite) data, respectively. The similarity of the distribution is a testament to our rigorous quality control process for the single-satellite FAC data (see Section 3.2). R1/R2 FACs are similar between the Swarm A and AC averaged data, with only minor differences in intensity and location. Differences are apparent throughout the noon MLT sector for all IMF clock angles. The intensity of the average FACs for a given IMF orientation are increased with respect to the large-scales shown in Figure 10. Though the large-scale patterns of Figure 10 are apparent at these scales, they are less coherent in Figure 11.

Figure 12 shows the FAC distributions at the smallest scale size addressed in this work, 50 km. Only single-satellite Swarm data provide observations at this scale size. Therefore, only Swarm A data are shown. R1/R2 FACs are dominant in the statistical results even at these scales, however, features at high-latitudes in the noon MLT sector and at auroral oval latitudes across the midnight MLT sector are more pronounced at 50 km scale size. Comparing Swarm A results across scales (Figures 10-12, i.e., 350, 150, and 50 km) differences are subtle. However, it is important to remember that these results represent statistical summaries of the magnitudes and distributions of the FACs, and will, therefore, not capture behavior occurring on short time scales, where differences between small- and

large-scales are most significant. It is more appropriate to examine scale size differences through other metrics.

Figure 13 shows sub-grid level variability for each scale size during purely northward (clock angle bin 0 ± 22.5°) and southward (90 ± 22.5°) IMF conditions. Bin variances become more substantial as scale size decreases (looking right to left in Figure 13), indicating the influence of small-scale activity. Swarm A FACs exhibit greater variance than AMPERE FACs at 350 km scale size (Figures 13d and e), yet smaller variance than Swarm AC at 150 km (Figures 13b and c). Enhanced variance characterizes the dayside region spanning MLATs between ∼65-80° (i.e., the ionospheric projection of the magnetospheric cusp, low-latitude boundary layer (LLBL), and mantle [*Vasyliunas*, 1979; *Newell et al.*, 1991; *Newell and Meng*, 1992]) for all IMF orientations. During northward conditions, this region is the distinguishing feature as variance in other MLT and MLAT locations is diminished. Southward conditions add drastically increased variability at the dusk, nightside, and dawn MLTs in a latitudinally expanded band between ∼55-70°. Only slight enhancements in variability are observed at the largest scales, and the enhancements are especially modest for AMPERE data.

In Figures 9-13 all data for a given pass are assigned to a single IMF orientation. Given that we already showed in the correlations in Figure 8 that northward IMF leads to increased spatial variability at local noon and that the small- and large-scales are more similar for southward conditions, increased variabilities during southward IMF in Figure 13 may be partially due to temporal averaging.

Figures 10-13 suggest that the magnetosphere is organized across larger spatial scales under southward IMF and that small-scale structure is, correspondingly, reduced. *Korth*

et al. [2011] compared large-scale FAC observations (from AMPERE) and large-scale magnetospheric simulations and found that observed and simulated FACs exhibit a great degree of similarity during southward IMF conditions, but that this similarity diminishes significantly as the IMF turns northward. They interpreted the difference to be due to the smaller area occupied by large-scale FACs during northward conditions such that small displacements produced relatively larger differences in their comparisons. Our results add small-scale information to this picture, and allow us to extend their conclusion. We showed that small-scale structure, while present during southward IMF, is more distinct from large-scales during northward IMF, which suggests that different characteristics across scales, not just displacement of large-scale currents, contribute to the FAC dependence on the IMF orientation.

The characteristics and controlling parameters of FACs presented to this point show distinct FAC behavior across scale sizes, and expanded influence of smaller scale FACs in the noon MLT sector and during conditions when the IMF is not dominated by the southward component. We next attempt to quantify the significance of the distinguishing behavior, attempting to answer the question, 'To what extent do mesoscale FACs depart from large-scale specification?'

4.4. Degree of Departure

All results presented to this point have been based solely on observations (i.e., from Swarm and AMPERE measurements). In this section we attempt to compare differences between observations and present large-scale understanding, using C2012 FACs to represent the present understanding, and, therefore, the background state in our definition of

'degree of departure' (see Section 3.5). All results in this section are based on comparisons between Swarm and AMPERE observations and the C2012 fitted FACs.

In Section 4.2.2 we addressed how the *form* of FACs changed with scale size when we compared Swarm to AMPERE. Here we attempt to determine how the form changes when we compare the observations with C2012 FACs. The results, organized in the same manner as Figure 8, are presented in Figure 14. The additional panel (Figure 14e) shows the average AMPERE-C2012 correlation coefficients in addition to the Swarm-C2012 results (Figures 14a-d).

The largest correlations between the observed and modeled FACs exist in the dawn and dusk sectors, as before. At 350 km scale, the observed and modeled FACs also show large correlations throughout the nightside, but these correlations disappear at smaller scales, reflecting the inability of R1/R2 FAC-focused modeling to capture night-time FACs and the increased influence of small-scale features to the overall FAC forms there. There is little to no similarity between observed and modeled FAC forms on the dayside at any scale, where the only correlations that exceed 0.4 occur between AMPERE and C2012 FACs when there is no northward component of the IMF. Further, the B_Y relationships discussed for Figure 8 are no longer well-pronounced. In fact, aside from reduced correlations for $+B_Z$, there appears to be a reduced dependence on the IMF clock angle overall when comparing Figures 8 and 14. The AMPERE data (and, in turn, the C2012 FACs) appear capable of capturing IMF clock angle dependencies, as has indeed been shown (Section 4.3.1), and that these map relatively well across scales, but that this is not true for the MLT dependencies. This may suggest that MLT is more important than the IMF

orientation in terms of the departure of FACs from large-scale specification, though this statement warrants further investigation.

Figure 15 further explores the degree of departure as a function of MLT, showing the average median absolute deviation (MAD) in 1 h bins. It is important to remember that these values represent the departure of the observed FACs from the C2012 modeled representation. Therefore, we are examining the residuals of the observations with respect to the large-scale R1/R2 currents.

We find that the C2012 R1/R2 FACs accurately capture the large-scale FAC observations (low MADs are recorded at dawn and dusk for Swarm A 350 km scale (orange trace) and AMPERE (light blue trace)). However, C2012 FACs less effectively describe dayside large-scale FACs (larger MADs for the same traces). A fundamentally distinct relationship occurs at 150 and 50 km scales. For the Swarm A 150 km (dark blue, trace), Swarm AC (yellow trace), and Swarm A 50 km (red trace) scales, the disagreement peaks in the dawn and dusk sectors, indicating small-scale influence above the large-scale R1/R2 FACs. The fact that the forms of the small- and large-scale FACs are most similar in these local time sectors (i.e., larger correlations, see Figure 14) illustrates that a distinction exists between accurately quantifying the *form* and *magnitude* of FACs. *Anderson et al.* [2017] illustrated this distinction, comparing AMPERE observations with results from various magnetospheric models for two geomagnetic storms. In Figure 15 a local peak occurs at these scales near noon local time. It is interesting to note that the MADs for Swarm AC are quantitatively closer to Swarm A 50 km than Swarm A 150 km. This is, in part, due to single- versus dual-satellite calculations and associated spatial and temporal effects, though other factors certainly contribute to the result.

Figure 16 shows the difference between FACs summed over each Swarm pass as a function of MLT. The pass-summed FACs are calculated from:

Median summed (+) FAC difference:

$$\text{Median}_N \left[\left(\sum_{l=1}^{L} \text{upward } J_r \text{Swarm A/AC, AMPERE} \right) - \left(\sum_{l=1}^{L} \text{upward } J_r \text{C2012} \right) \forall n \right], \quad (2)$$

and:

Median summed (-) FAC difference:

$$\text{Median}_N \left[\left(\left| \sum_{l=1}^{L} \text{downward } J_r \text{Swarm A/AC, AMPERE} \right| \right) - \left(\left| \sum_{l=1}^{L} \text{downward } J_r \text{C2012} \right| \right) \forall n \right] \quad (3)$$

where J_r is the FAC density in μA m^{-2}, L is the total number of data points in the n^{th} Swarm pass, N is the total number of Swarm passes, and Median_N indicates that the median over all passes ($\forall n$) is taken. We calculate the median values for each 1 h MLT sector and plot the results in Figure 16 for each scale size. In Figure 16 polar plots no longer show MLT-MLAT distributions. Instead, MLT-difference magnitudes are plotted, where the magnitude of the difference is indicated by the distance from the center of the plot. For clarity, the size and color of the data points also indicate the magnitude of the difference. In MLT locations where the positive and negative difference magnitudes overlap the larger difference is plotted on top.

Differences between the observed and C2012 FACs illustrate a consistent pattern in MLT: a horseshoe shape with the greatest differences occurring throughout the dayside. The level of departure becomes more severe for smaller scales, reaching > 20 μA m^{-2} for local times spanning dawn, through noon, to dusk for Swarm A 50 km scales. For all Swarm A results (Figures 16a-c) differences between the upward currents (shown in red) are greater than those for the downward currents (shown in blue) throughout the

dayside, but in the premidnight sector the opposite is true. In fact, for each comparison the difference for the downward FACs exceeds that of the upward FACs in the premidnight sector. Across the midnight meridian all results show the opposite case for at least one hour local time. Therefore, the observations and C2012 are in greater disagreement for the downward currents in the premidnight sector, and, at least for one hour MLT, in greater disagreement for the upward currents in the postmidnight sector. This may indicate the influence of the substorm current wedge, where the FACs are complex and typically smaller scale [*Murphy et al.*, 2013]. Ultimately, the departure data shown in Figure 16 reveals that FAC relationships do not trivially map across scales.

Figure 16 emphasizes that large-scale R1/R2 FACs may not, in certain locations, be sufficient to accurately describe FAC dynamics. We show that these effects are most pronounced in the noon and midnight LT sectors, corroborating conclusions drawn in previous work [*Neubert and Christiansen*, 2003]. Our results suggest that small- and mesoscale FACs likely play a significant role in critical geospace phenomena in these MLTs. We discuss this further in Section 5.3.

5. Discussion

In this section, we extend the discussion of our results in three specific directions: 1) comparison with previous multi-scale FAC studies; 2) implications of our discoveries for the MIT system, focusing on the possible connections between multi-scale FACs and 'anomalous' neutral density and Joule heating behavior in the ionosphere-thermosphere (IT); and 3) future considerations. We use these directions to contribute to the current understanding of multi-scale FACs and their impact and to identify important future work.

5.1. Summer-to-Winter ratio

One metric that has been widely used to quantify different specifications of FACs is the total FAC summer-to-winter ratio [*Juusola et al.*, 2009], and we use it here to assess the effect of multi-scale FACs in the context of the global current system. Investigation of the summer-to-winter relationship of FACs has not before been examined as a function of scale size. To calculate the total FACs flowing in each season we follow the approach of *Coxon et al.* [2014a] where FAC densities are binned and multiplied by the bin area to give an integrated value. We use the same equal area bins from above in this process and define the summer and winter seasons by a 120 day period centered on the summer and winter solstices, respectively [*Juusola et al.*, 2009].

Table 2 gives results from previous estimates of the ratio and those found using our database. We find general agreement with previous estimates. Summer FACs exceed winter FACs by a factor of ∼1.3-2.0 [*Fujii et al.*, 1981; *Papitashvili et al.*, 2002; *Christiansen et al.*, 2002; *Ridley*, 2007; *Juusola et al.*, 2009]. The particular factor depends on the data set and resolution used in the calculations. This is true for our database, and we, therefore, focus on the relative relationship between scales which is not a function of these parameters. We do not find a significant scale size dependency of the summer-to-winter ratio. Perhaps this is due to the effects of small-scales averaging out in these calculations, or it may indicate that the seasonal ratio is independent of scale size. We suggest that small-scale FACs may increase in relative importance on shorter time scales.

5.2. Net FACs

The sum of FACs for any given pass is frequently non-zero (i.e., there is a net current flowing either into or out of the ionosphere). Net currents are closed through horizontal

paths in the IT system, and are important to the dynamics of the entire system [*Kamide*, 1982]. Differences in location and magnitude of the net currents drive different system behavior, and are, therefore, a critical parameter.

We calculate the net currents according to:

Average net summed FACs:

$$\frac{1}{N}\sum_{n=1}^{N}\left[\left(\sum_{l=1}^{L}\text{upward } J_r\text{Swarm A/AC, AMPERE}\right)+\left(\sum_{l=1}^{L}\text{downward } J_r\text{Swarm A/AC, AMPERE}\right)\right] \quad (4$$

where N is the total number of passes and L is the number of data points in pass n. Note that the downward currents will always be negative so that Equation 4 is equivalent to subtracting the absolute value of the downward FACs from the upward FACs. Figure 17 illustrates the MLT dependence and magnitude of the net currents for our database. We calculate average values in two ways: 1) binning the data into four, six hour MLT bins (midnight: 2100-0300, dawn: 0300-0900, noon: 0900-1500, and dusk: 1500-2100; Figure 17a), and 2) in one hour MLT bins (Figure 17b).

Figure 17a gives the net FAC results in the four key MLT sectors (from left to right on the figure): midnight, dawn, noon, and dusk. The largest net FACs for all scales occur in the dusk sector, where a net current out of the ionosphere (R1 sense) is observed. Comparable, but notably smaller, net FACs are directed into the ionosphere at dawn. Our results uniformly give greater overall current flowing out of the ionosphere at dusk than flowing into the ionosphere at dawn. The differences between the net currents at dusk and those at dawn ([μA m^{-2}]) are +8.5 (Swarm A 50 km), +8.5 (Swarm A 150 km), +10.7 (Swarm AC), +8.6 (Swarm A 350 km), and +6.0 (AMPERE). These dawn-dusk imbalances must close through the ionosphere. Large-scale FACs typically close either in the auroral region between the R1/R2 FACs at dawn and dusk or across the polar

cap (see Figure 1). *Le et al.* [2010] also found that the net currents follow a R1 sense at dawn and dusk, and calculated that these net currents followed the latter path, resulting in significant Pedersen closure currents across the polar cap. However, the large-scale closure paths need not be the only solutions. Significant small-scale FAC activity in the noon and midnight MLT sectors may alter the system of horizontal ionospheric currents. Figure 17a also provides the net currents in these local time sectors, showing a slight average net current flowing into the ionosphere at midnight and a more complex picture at noon. The average current is directed away from the ionosphere at noon for all estimates except Swarm AC, which instead shows a strong net current in the opposite sense. The cause of the discrepancy is explained in part in Figure 17b, which shows the values as a function of MLT in 1 h MLT bins. The Swarm AC net FACs are shifted to later MLTs with respect to the other estimates (a shift toward the right in the middle panel with respect to each other panel). This shift causes the positive net currents at 1500 MLT in the other estimates to occur outside of the noon MLT sector (0900-1500) used for Figure 17a for Swarm AC estimates. We note that the difference observed for the Swarm AC estimates is more nuanced than a simple shift to the right with respect to the other estimates. Though Figure 17b cannot offer a definitive explanation of the cause of the differences, one likely contributor is more intense FACs estimated by Swarm AC poleward of the dayside R1/R2 FACs (compare, for instance, Figures 11a and b). These poleward FACs would affect the average net summed FACs shown in Figure 17. This is illustrative of the differences between scales in the noon MLT sector and underscores the potential impacts of these differences. Overall, Figure 17 emphasizes the importance of future investigation

into the effects of the midnight and noon MLT sectors due to multi-scale FACs on the global ionospheric current system.

Values to the right of the legend in Figure 17a give the global net currents. AMPERE estimates the FACs to be nearly balanced (-0.4), the Swarm A estimates yield a net FAC away from the ionosphere, and Swarm AC, likely due to the difference in the noon sector, estimates a net current into the ionosphere. Clearly, smaller scales create a different picture of the global FACs.

In Figure 17b large-scale net FACs (bottom two panels in Figure 17b) show general agreement with a similar investigation performed by *Peria et al.* [2013] using a different approach and database (the Fast Auroral SnapshoT Explorer, FAST - their Figure 4). The agreement gives credence to our approach. With the exception of the shift toward later MLTs for Swarm AC discussed above, the trend in the net FACs at small and large scales are in agreement (net summed FACs into the ionosphere from ∼1-11 MLT and away from the ionosphere from ∼13-23 MLT). However, the magnitude of the imbalance between upward and downward FACs is enhanced at both the small (50 km, top panel Figure 17b) and mesoscales (150 km, second panel Figure 17b). Given that the trend of net currents is augmented by the smaller scales, rather than significantly altered, we infer that the small and mesoscales contribute to the global current system and are not simply small structures that are closed locally in the ionosphere. This is new evidence that supports the inferences of *Peria et al.* [2013].

5.3. Impact on IT system

We next explore the impact of multi-scale FACs on the IT system. FACs are the main mechanism for energy and momentum transfer from the magnetosphere to the IT system.

In the ionosphere, FACs drive a system of horizontal Hall and Pedersen currents, which, in turn, exert control over the IT system dynamics. In the absence of conductivity gradients, Hall currents are divergence free and close completely in the ionosphere [*Sofko et al.*, 1995]. In this case, FACs are closed via Pedersen currents, leading to Joule heating and variability of electron density, neutral composition, and temperature [*Banks et al.*, 1981]. Though the qualitative process is known there are numerous outstanding questions whose closure likely require multi-scale understanding. We will consider the following question in the present discussion, 'Is there a physical connection between the areas of greatest difference between small-, meso-, and large-scale FACs (i.e., along the noon-midnight local time meridian, see Figure 16) and locations of 'anomalous' Joule heating and neutral density enhancements [*Lühr et al.*, 2004; *Deng et al.*, 2013]?'

Given our results in the context of previous characterization of Joule heating and neutral density in the noon-midnight meridian, we suggest the answer is yes. *Neubert and Christiansen* [2003] found a clear occurrence maximum for small-scale FACs in the cusp and adjacent regions from a survey of Øersted satellite data. Our results corroborate and extend their result, showing that small- and mesoscale FACs are highly variable (i.e., dynamic) in this local time sector (Figure 5) and that the degree of departure from large-scale FACs is more severe there (Figure 16). These smaller scale FACs would plausibly contribute to enhanced variability of the ionospheric electric field, which *Codrescu et al.* [1995] and *Deng and Ridley* [2007] both demonstrated contributes quite significantly to Joule heating. *Neubert and Christiansen* [2003] recognized this connection and concluded that small-scale FACs are likely associated with significant local heating of the IT system. Further, *Foster et al.* [1983] conducted a comprehensive investigation of Joule heating

using the AE-C satellite and discovered the overall heating pattern is horseshoe-shaped with the dawn-dusk and dayside regions contributing the largest heat input. Their result is remarkably similar in form to the degree of departure results we presented in Figure 16, an enticing similarity to motivate further investigation.

The inferences above are based on correspondences between the locations of small-scale and mesoscale FACs and Joule heating, but are not sufficient to establish a physical connection between the two nor between FACs and neutral density enhancement. However, there is evidence from simultaneous observations of FACs and neutral density enhancements that these processes are physically connected. *Lühr et al.* [2004] found that whenever very intense small-scale (defined in their work to be ∼1 km) FAC structures were present, neutral density enhancements also occurred. They also found that neutral density enhancements are nearly always observed by the CHAMP satellite upon passage through the geomagnetic cusp region.

We may speculate, to great potential impact, that small- and mesoscale FACs are related to frequent heating and neutral density enhancements in the ionospheric cusp local time sector, and that similar relationships may exist at other MLTs. Simultaneous observations of FACs, ionospheric currents, electric fields, and thermospheric neutral densities are needed to quantify the relationship and establish physical causation. Relationships are also heavily dependent on accurate characterization of the ionospheric conductivity distributions [*McGranaghan et al.*, 2016]. Clearly, however, FACs across multiple scales are relevant to the IT system.

We do not address Alfvénic FACs (micro-scale), which are beneath the scale measured by the Swarm and AMPERE data. However, Alfvénic fluctuations may be an integral

component of the relationship between FACs and IT heating [*Lühr et al.*, 2004; *Zhang et al.*, 2015].

Table 3 summarizes the significance of the extensive results presented in this manuscript and provides a roadmap to the primary figures in this paper where each conclusion is supported.

5.4. Future considerations

Given the important questions raised by this study, we provide a discussion of the promising avenues of future work that are enabled by and have the opportunity to extend our results.

Our results can guide efforts for improved FAC modeling. Figure 14 showed linear correlations between observed and background R1/R2 FACs, represented by C2012 FACs, and revealed areas where current large-scale representation is sufficient to describe the form of the FACs at all scales (i.e., where relatively strong linear relationships between scales existed to parameterize small-scales given large-scale knowledge) and highlighted areas where new understanding is required to accurately model FACs across scales (i.e., where large-scales will not necessarily provide useful information to quantify smaller scales). In other words, these results can help direct modeling efforts as to where increased resolution may be sufficient and where new physical understanding is required. We note that lack of correlation in Figures 8 and 14 does not imply that no relationship exists. It does, however, imply that a strong linear relationship does not exist, or, alternatively, that relationships for these conditions are likely nonlinear. Nonlinear relationships may exist for all conditions, but may only become apparent or become relatively more important when the strength of the linear relationship is diminished.

We have primarily investigated statistical results for multi-scale FACs. Summarizing these data statistically inevitably reduces the information content of the original data. Therefore, future work will attempt to augment these statistical findings with case study results. Such case studies should make use of multi-instrument observations to provide complementary FAC data and facilitate closure of the questions raised in Section 5. Moreover, we utilized a data-driven approach in this work and suggest that a key area of future research should be to apply advanced techniques to learn critical new relationships in the data that are consistent with both statistical and detailed case study data.

Already, innovative techniques, such as network analysis [*Boccaletti et al.*, 2006], are being applied to ionospheric data sets and discovering relationships that are complementary and distinct from relationships discovered with more traditional approaches [*Dods et al.*, 2015, 2017; *McGranaghan et al.*, 2017; *Shore et al.*, 2017]. These studies illustrate the importance of data-driven methodologies to augment traditional approaches

6. Conclusions

Using an extensive and unique database of multi-scale field aligned currents (FACs) compiled from the European Space Agency's Swarm satellites and the Advanced Magnetosphere and Planetary Electrodynamics Response Experiment (AMPERE), we have conducted a comprehensive analysis. We examined the repeatable behavior of FACs across a range of scales in terms of the statistical characteristics, and the dependence on the interplanetary magnetic field (IMF) orientation, a dominant controlling factor. This work, therefore, represents the first comprehensive, cross-platform investigation of FAC characteristics across scales. We utilized our rich database of FAC information to also investigate the degree to which FACs at different scales depart from the nominal large-scale specifi-

cation. We quantified the results by defining the 'degree of departure,' which allowed the description of the amount and intensity of the disagreement between the observed and modeled FACs.

In general, we discovered significant differences in the characteristics and behavior of FACs resolved at small-scales (∼10-150 km, <1° latitudinal width) and mesoscales (∼150-250 km, 1-2° latitudinal width), from those only resolved at larger scales (>250 km). The following is a concise summary of our results:

- The characteristics and dependence on controlling parameters of FACs do not trivially map between scales.
- There exists a local time dependence in the relationships between FAC scales: linear relationships may exist near dawn and dusk local times under southward IMF orientations (i.e., stronger magnetospheric driving), while noon and midnight local times do not exhibit linear relationships, and the effect is pronounced when the IMF is not southward.
- When analyzed at different scales, remarkably distinct FAC behavior is the hallmark of the dayside high-latitude region, and corresponds to locations of increased Joule heating and 'anomalous' neutral density enhancements. The correspondence suggests important ionosphere-thermosphere (IT) impacts.

We suggest that both an understanding of as yet unknown relationships, which can possibly be discovered through machine learning-based approaches, and increased resolution of models are required to address the multi-scale FAC complexities. We have provided a rigorous and comprehensive step toward data-driven discovery of the salient multi-scale FAC relationships and outlined promising next steps. Given the statistical nature of our results, among the important next steps are to analyze multi-scale FACs using less tem-

poral averaging and in the context of multi-instrument observations through detailed case studies. Our database is well suited for such studies.

Acknowledgments. This research was supported by the NASA Living With a Star Jack Eddy Postdoctoral Fellowship Program, administered by the University Corporation for Atmospheric Research and coordinated through the Cooperative Programs for the Advancement of Earth System Science (CPAESS). Portions of this research were carried out at the Jet Propulsion Laboratory, California Institute of Technology, under a contract with the National Aeronautics and Space Administration. C. Forsyth was supported by a Natural Environment Research Council Independent Research Fellowship (NE/N014480/1) and ESA contract 4000114090 (Swarm Investigation of the Role of High-Frequency (0.1-5Hz) ULF Waves in Magnetosphere-Ionosphere Coupling) Swarm+Support to Science Element.

We gratefully acknowledge the European Space Agency and the Swarm Science Team for providing the Level 2 field aligned current data (accessible at https://earth.esa.int/web/guest/swarm/data-access) and usage support. For the Iridium-derived AMPERE data (accessible at http://ampere.jhuapl.edu/), we acknowledge the AMPERE Science Center at the Johns Hopkins University Applied Physics Laboratory. We acknowledge the use of NASA/GSFC's Space Physics Data Facility's CDAweb service to obtain the OMNI data (accessible at http://omniweb.gsfc.nasa.gov/).

The authors would like to specifically acknowledge and thank Olga Verkhoglyadova for her thoughtful and valuable conversations to improve this manuscript.

References

Anderson, B. J., K. Takahashi, and B. A. Toth (2000), Sensing global Birkeland currents with iridium engineering magnetometer data, *Geophysical Research Letters*, *27*(24), 4045–4048, doi:10.1029/2000GL000094.

Anderson, B. J., H. Korth, C. L. Waters, D. L. Green, and P. Stauning (2008), Statistical Birkeland current distributions from magnetic field observations by the Iridium constellation, *Annales Geophysicae*, *26*(3), 671–687, doi:10.5194/angeo-26-671-2008.

Anderson, B. J., H. Korth, C. L. Waters, D. L. Green, V. G. Merkin, R. J. Barnes, and L. P. Dyrud (2014), Development of large-scale Birkeland currents determined from the Active Magnetosphere and Planetary Electrodynamics Response Experiment, *Geophysical Research Letters*, *41*(9), 2014GL059941, doi:10.1002/2014GL059941.

Anderson, B. J., H. Korth, D. T. Welling, V. G. Merkin, M. J. Wiltberger, J. Raeder, R. J. Barnes, C. L. Waters, A. A. Pulkkinen, and L. Rastaetter (2017), Comparison of predictive estimates of high-latitude electrodynamics with observations of global-scale Birkeland currents, *Space Weather*, *15*(2), 2016SW001529, doi:10.1002/2016SW001529.

Banks, P. M., J. C. Foster, and J. R. Doupnik (1981), Chatanika Radar observations relating to the latitudinal and local time variations of Joule heating, *Journal of Geophysical Research: Space Physics*, *86*(A8), 6869–6878, doi:10.1029/JA086iA08p06869.

Birkeland, K. R. (1908), *The Norwegian Aurora Polaris Expedition 1902-1903*, vol. 1, H. Aschelhoug and Co., Christiania, Norway.

Birkeland, K. R. (1913), *The Norwegian Aurora Polaris Expedition 1902-1903*, vol. 2, H. Aschelhoug and Co., Christiania, Norway.

Boccaletti, S., V. Latora, Y. Moreno, M. Chavez, and D.-U. Hwang (2006), Complex networks: Structure and dynamics, *Physics Reports*, *424*(45), 175 – 308, doi:http://dx.doi.org/10.1016/j.physrep.2005.10.009.

Carter, J. A., S. E. Milan, J. C. Coxon, M.-T. Walach, and B. J. Anderson (2016), Average field-aligned current configuration parameterized by solar wind conditions, *Journal of Geophysical Research: Space Physics*, *121*(2), 2015JA021567, doi:10.1002/2015JA021567.

Cattell, C., J. Dombeck, W. Peria, R. Strangeway, R. Elphic, and C. Carlson (2003), Fast Auroral Snapshot observations of the dependence of dayside auroral field-aligned currents on solar wind parameters and solar illumination, *Journal of Geophysical Research: Space Physics*, *108*(A3), 1112, doi:10.1029/2001JA000321.

Chaston, C. C., J. W. Bonnell, C. W. Carlson, J. P. McFadden, R. E. Ergun, and R. J. Strangeway (2003), Properties of small-scale Alfvèn waves and accelerated electrons from FAST, *Journal of Geophysical Research: Space Physics*, *108*(A4), 8003, doi:10.1029/2002JA009420.

Christiansen, F., V. O. Papitashvili, and T. Neubert (2002), Seasonal variations of high-latitude field-aligned currents inferred from Ørsted and Magsat observations, *Journal of Geophysical Research: Space Physics*, *107*(A2), SMP 5–1–SMP 5–13, doi:10.1029/2001JA900104.

Clausen, L. B. N., J. B. H. Baker, J. M. Ruohoniemi, S. E. Milan, and B. J. Anderson (2012), Dynamics of the region 1 Birkeland current oval derived from the Active Magnetosphere and Planetary Electrodynamics Response Experiment (AMPERE), *Journal of Geophysical Research: Space Physics*, *117*(A6), A06233, doi:10.1029/2012JA017666.

Codrescu, M. V., T. J. Fuller-Rowell, and J. C. Foster (1995), On the importance of E-field variability for Joule heating in the high-latitude thermosphere, *Geophysical Research Letters*, *22*(17), 2393–2396, doi:10.1029/95GL01909.

Cowley, S. W. H. (2013), *Magnetosphere-Ionosphere Interactions: A Tutorial Review*, pp. 91–106, American Geophysical Union, doi:10.1029/GM118p0091.

Coxon, J. C., S. E. Milan, L. B. N. Clausen, B. J. Anderson, and H. Korth (2014a), The magnitudes of the regions 1 and 2 Birkeland currents observed by AMPERE and their role in solar wind-magnetosphere-ionosphere coupling, *Journal of Geophysical Research: Space Physics*, *119*(12), 2014JA020138, doi:10.1002/2014JA020138.

Coxon, J. C., S. E. Milan, L. B. N. Clausen, B. J. Anderson, and H. Korth (2014b), A superposed epoch analysis of the regions 1 and 2 Birkeland currents observed by AMPERE during substorms, *Journal of Geophysical Research: Space Physics*, *119*(12), 2014JA020500, doi:10.1002/2014JA020500.

Coxon, J. C., S. E. Milan, J. A. Carter, L. B. N. Clausen, B. J. Anderson, and H. Korth (2016), Seasonal and diurnal variations in AMPERE observations of the Birkeland currents compared to modeled results, *Journal of Geophysical Research: Space Physics*, *121*(5), 2015JA022050, doi:10.1002/2015JA022050.

Deng, Y., and A. J. Ridley (2007), Possible reasons for underestimating Joule heating in global models: E field variability, spatial resolution, and vertical velocity, *Journal of Geophysical Research: Space Physics*, *112*(A9), A09308, doi:10.1029/2006JA012006.

Deng, Y., T. J. Fuller-Rowell, A. J. Ridley, D. Knipp, and R. E. Lopez (2013), Theoretical study: Influence of different energy sources on the cusp neutral density enhancement, *Journal of Geophysical Research: Space Physics*, *118*(5), 2340–2349, doi:

10.1002/jgra.50197.

Dods, J., S. C. Chapman, and J. W. Gjerloev (2015), Network analysis of geomagnetic substorms using the SuperMAG database of ground-based magnetometer stations, *Journal of Geophysical Research: Space Physics*, *120*(9), 2015JA021456, doi: 10.1002/2015JA021456.

Dods, J., S. C. Chapman, and J. W. Gjerloev (2017), Characterising the ionospheric current pattern response to southward and northward IMF turnings with dynamical SuperMAG correlation networks, *Journal of Geophysical Research: Space Physics*, 2016JA023686, doi:10.1002/2016JA023686.

Dungey, J. W. (1961), Interplanetary Magnetic Field and the Auroral Zones, *Phys. Rev. Lett.*, *6*, 47–48, doi:10.1103/PhysRevLett.6.47.

Fear, R. C., M. Palmroth, and S. E. Milan (2012), Seasonal and clock angle control of the location of flux transfer event signatures at the magnetopause, *Journal of Geophysical Research: Space Physics*, *117*(A4), A04202, doi:10.1029/2011JA017235.

Forsyth, C., I. J. Rae, I. R. Mann, and I. P. Pakhotin (2017), Identifying intervals of temporally invariant field-aligned currents from Swarm: Assessing the validity of single-spacecraft methods, *Journal of Geophysical Research: Space Physics*, *122*(3), 2016JA023708, doi:10.1002/2016JA023708.

Foster, J. C., J.-P. St.-Maurice, and V. J. Abreu (1983), Joule heating at high latitudes, *Journal of Geophysical Research: Space Physics*, *88*(A6), 4885–4897, doi: 10.1029/JA088iA06p04885.

Fujii, R., T. Iijima, T. A. Potemra, and M. Sugiura (1981), Seasonal dependence of large-scale Birkeland currents, *Geophysical Research Letters*, *8*(10), 1103–1106, doi:

10.1029/GL008i010p01103.

Fuller-Rowell, T. J., and D. S. Evans (1987), Height-integrated Pedersen and Hall conductivity patterns inferred from the TIROS-NOAA satellite data, *Journal of Geophysical Research: Space Physics*, *92*(A7), 7606–7618, doi:10.1029/JA092iA07p07606.

Gjerloev, J. W., S. Ohtani, T. Iijima, B. Anderson, J. Slavin, and G. Le (2011), Characteristics of the terrestrial field-aligned current system, *Annales Geophysicae*, *29*(10), 1713–1729, doi:10.5194/angeo-29-1713-2011.

Hardy, D. (1985), A statistical model of auroral electron precipitation, *Journal of Geophysical Research*, *90*(A5), 4229–4248.

Hardy, D. A., M. S. Gussenhoven, R. Raistrick, and W. J. McNeil (1987), Statistical and functional representations of the pattern of auroral energy flux, number flux, and conductivity, *Journal of Geophysical Research: Space Physics*, *92*(A11), 12,275–12,294, doi:10.1029/JA092iA11p12275.

Hasunuma, T., T. Nagatsuma, R. Kataoka, Y. Takahashi, H. Fukunishi, A. Matsuoka, and A. Kumamoto (2008), Statistical study of polar distribution of mesoscale field-aligned currents, *Journal of Geophysical Research: Space Physics*, *113*(A12), A12214, doi:10.1029/2008JA013358.

He, M., J. Vogt, H. Lhr, E. Sorbalo, A. Blagau, G. Le, and G. Lu (2012), A high-resolution model of field-aligned currents through empirical orthogonal functions analysis (MFACE), *Geophysical Research Letters*, *39*(18), L18105, doi:10.1029/2012GL053168.

Hruška, A. (1981), Closure of field-aligned currents in the ionosphere, *Astrophysics and Space Science*, *77*(1), 159–165, doi:10.1007/BF00648763.

Huang, C. Y., Y.-J. Su, E. K. Sutton, D. R. Weimer, and R. L. Davidson (2014), Energy coupling during the August 2011 magnetic storm, *Journal of Geophysical Research: Space Physics*, *119*(2), 2013JA019297, doi:10.1002/2013JA019297.

Humberset, B. K., J. W. Gjerloev, M. Samara, and R. G. Michell (2017), Scale size-dependent characteristics of the nightside aurora, *Journal of Geophysical Research: Space Physics*, *122*(2), 2016JA023695, doi:10.1002/2016JA023695.

Iijima, T., and T. A. Potemra (1976a), The amplitude distribution of field-aligned currents at northern high latitudes observed by Triad, *Journal of Geophysical Research*, *81*(13), 2165–2174, doi:10.1029/JA081i013p02165.

Iijima, T., and T. A. Potemra (1976b), Field-aligned currents in the dayside cusp observed by Triad, *Journal of Geophysical Research*, *81*(34), 5971–5979, doi:10.1029/JA081i034p05971.

Iijima, T., and T. A. Potemra (1978), Large-scale characteristics of field-aligned currents associated with substorms, *Journal of Geophysical Research: Space Physics*, *83*(A2), 599–615, doi:10.1029/JA083iA02p00599.

Juusola, L., K. Kauristie, O. Amm, and P. Ritter (2009), Statistical dependence of auroral ionospheric currents on solar wind and geomagnetic parameters from 5 years of CHAMP satellite data, *Annales Geophysicae*, *27*(3), 1005–1017, doi:10.5194/angeo-27-1005-2009.

Juusola, L., S. E.?Milan, M. Lester, A. Grocott, and S. M.?Imber (2014), Interplanetary magnetic field control of the ionospheric field-aligned current and convection distributions, *Journal of Geophysical Research: Space Physics*, *119*(4), 3130–3149, doi:10.1002/2013JA019455.

Kamide, Y. (1982), The relationship between field-aligned currents and the auroral electrojets: A review, *Space Science Reviews*, *31*(2), 127–243, doi:10.1007/BF00215281.

Korth, H., B. J. Anderson, and C. L. Waters (2010), Statistical analysis of the dependence of large-scale Birkeland currents on solar wind parameters, *Annales Geophysicae*, *28*(2), 515–530, doi:10.5194/angeo-28-515-2010.

Korth, H., L. Rastätter, B. J. Anderson, and A. J. Ridley (2011), Comparison of the observed dependence of large-scale Birkeland currents on solar wind parameters with that obtained from global simulations, *Annales Geophysicae*, *29*(10), 1809–1826, doi:10.5194/angeo-29-1809-2011.

Korth, H., Y. Zhang, B. J. Anderson, T. Sotirelis, and C. L. Waters (2014), Statistical relationship between large-scale upward field-aligned currents and electron precipitation, *Journal of Geophysical Research: Space Physics*, *119*(8), 2014JA019961, doi:10.1002/2014JA019961.

Kustov, A. V., W. B. Lyatsky, G. J. Sofko, and L. Xu (2000), Field-aligned currents in the polar cap at small imf bz and by inferred from superdarn radar observations, *Journal of Geophysical Research: Space Physics*, *105*(A1), 205–214, doi:10.1029/1999JA900428.

Le, G., Y. Wang, J. A. Slavin, and R. J. Strangeway (2009), Space technology 5 multipoint observations of temporal and spatial variability of field-aligned currents, *Journal of Geophysical Research: Space Physics*, *114*(A8), A08206, doi:10.1029/2009JA014081.

Le, G., J. A. Slavin, and R. J. Strangeway (2010), Space Technology 5 observations of the imbalance of regions 1 and 2 field-aligned currents and its implication to the cross-polar cap Pedersen currents, *Journal of Geophysical Research: Space Physics*, *115*(A7), A07202, doi:10.1029/2009JA014979.

Lühr, H., J. Warnecke, L. J. Zanetti, P. A. Lindqvist, and T. J. Hughes (1994), Fine structure of field-aligned current sheets deduced from spacecraft and ground-based observations: Initial FREJA results, *Geophysical Research Letters*, *21*(17), 1883–1886, doi:10.1029/94GL01278.

Lühr, H., M. Rother, W. Khler, P. Ritter, and L. Grunwaldt (2004), Thermospheric upwelling in the cusp region: Evidence from CHAMP observations, *Geophysical Research Letters*, *31*(6), L06805, doi:10.1029/2003GL019314.

Lühr, H., J. Park, J. W. Gjerloev, J. Rauberg, I. Michaelis, J. M. G. Merayo, and P. Brauer (2015), Field-aligned currents' scale analysis performed with the swarm constellation, *Geophysical Research Letters*, *42*(1), 2014GL062453, doi:10.1002/2014GL062453.

McDiarmid, I., J. Burrows, and M. D. Wilson (1980), Comparison of magnetic field perturbations and solar electron profiles in the polar cap, *Journal of Geophysical Research: Space Physics*, *85*(A3), 1163–1170, doi:10.1029/JA085iA03p01163.

McGranaghan, R., D. J. Knipp, T. Matsuo, and E. Cousins (2016), Optimal interpolation analysis of high-latitude ionospheric Hall and Pedersen conductivities: Application to assimilative ionospheric electrodynamics reconstruction, *Journal of Geophysical Research: Space Physics*, *121*(5), 2016JA022486, doi:10.1002/2016JA022486.

McGranaghan, R. M. (2016), Determining global ionospheric conductivity in the satellite and data assimilation age and assessing its influence on the magnetosphere-ionosphere-thermosphere system, dissertation, University of Colorado, Boulder, Boulder, Colorado.

McGranaghan, R. M., A. J. Mannucci, O. Verkhoglyadova, and N. Malik (2017), Finding multiscale connectivity in our geospace observational system: Network analysis of total electron content, *Journal of Geophysical Research: Space Physics*, 2017JA024202, doi:

10.1002/2017JA024202.

Milan, S. E., J. A. Carter, H. Korth, and B. J. Anderson (2015), Principal component analysis of Birkeland currents determined by the Active Magnetosphere and Planetary Electrodynamics Response Experiment, *Journal of Geophysical Research: Space Physics*, *120*(12), 2015JA021680, doi:10.1002/2015JA021680.

Murphy, K. R., I. R. Mann, I. J. Rae, C. L. Waters, H. U. Frey, A. Kale, H. J. Singer, B. J. Anderson, and H. Korth (2013), The detailed spatial structure of field-aligned currents comprising the substorm current wedge, *Journal of Geophysical Research: Space Physics*, *118*(12), 7714–7727, doi:10.1002/2013JA018979.

Neubert, T., and F. Christiansen (2003), Small-scale, field-aligned currents at the top-side ionosphere, *Geophysical Research Letters*, *30*(19), 2010, doi:10.1029/2003GL017808.

Newell, P. T., and C.-I. Meng (1992), Mapping the dayside ionosphere to the magnetosphere according to particle precipitation characteristics, *Geophysical Research Letters*, *19*(6), 609–612, doi:10.1029/92GL00404.

Newell, P. T., W. J. Burke, E. R. Snchez, C.-I. Meng, M. E. Greenspan, and C. R. Clauer (1991), The low-latitude boundary layer and the boundary plasma sheet at low altitude: Prenoon precipitation regions and convection reversal boundaries, *Journal of Geophysical Research: Space Physics*, *96*(A12), 21,013–21,023, doi:10.1029/91JA01818.

Newell, P. T., T. Sotirelis, and S. Wing (2009), Diffuse, monoenergetic, and broadband aurora: The global precipitation budget, *Journal of Geophysical Research: Space Physics*, *114*(A9), n/a–n/a, doi:10.1029/2009JA014326.

Newell, P. T., T. Sotirelis, and S. Wing (2010), Seasonal variations in diffuse, monoenergetic, and broadband aurora, *Journal of Geophysical Research: Space Physics*, *115*(A3),

n/a–n/a, doi:10.1029/2009JA014805.

Ohtani, S., G. Ueno, and T. Higuchi (2005), Comparison of large-scale field-aligned currents under sunlit and dark ionospheric conditions, *Journal of Geophysical Research: Space Physics*, *110*(A9), A09230, doi:10.1029/2005JA011057.

Olsen, N., E. Friis-Christensen, R. Floberghagen, P. Alken, C. D. Beggan, A. Chulliat, E. Doornbos, J. T. da Encarnação, B. Hamilton, G. Hulot, J. van den IJssel, A. Kuvshinov, V. Lesur, H. Lühr, S. Macmillan, S. Maus, M. Noja, P. E. H. Olsen, J. Park, G. Plank, C. Püthe, J. Rauberg, P. Ritter, M. Rother, T. J. Sabaka, R. Schachtschneider, O. Sirol, C. Stolle, E. Thébault, A. W. P. Thomson, L. Tøffner-Clausen, J. Velímský, P. Vigneron, and P. N. Visser (2013), The Swarm Satellite Constellation Application and Research Facility (SCARF) and Swarm data products, *Earth, Planets and Space*, *65*(11), 1, doi:10.5047/eps.2013.07.001.

Papitashvili, V. O., F. Christiansen, and T. Neubert (2002), A new model of field-aligned currents derived from high-precision satellite magnetic field data, *Geophysical Research Letters*, *29*(14), 28–1–28–4, doi:10.1029/2001GL014207.

Peria, W. J., C. W. Carlson, R. E. Ergun, J. P. McFadden, J. Bonnell, R. C. Elphic, and R. J. Strangeway (2013), *Characteristics of Field-Aligned Currents Near the Auroral Acceleration Region: Fast Observations*, pp. 181–189, American Geophysical Union, doi:10.1029/GM118p0181.

Ridley, A. J. (2007), Effects of seasonal changes in the ionospheric conductances on magnetospheric field-aligned currents, *Geophysical Research Letters*, *34*(5), L05101, doi:10.1029/2006GL028444.

Ritter, P., H. Lühr, and J. Rauberg (2013), Determining field-aligned currents with the Swarm constellation mission, *Earth, Planets and Space*, *65*(11), 9, doi: 10.5047/eps.2013.09.006.

Ruohoniemi, J. M., and K. B. Baker (1998), Large-scale imaging of high-latitude convection with Super Dual Auroral Radar Network HF radar observations, *Journal of Geophysical Research: Space Physics*, *103*(A9), 20,797–20,811, doi:10.1029/98JA01288.

Saflekos, N., and T. Potemra (1980), The orientation of Birkeland current sheets in the dayside polar region and its relationship to the IMF, *Journal of Geophysical Research: Space Physics*, *85*(A5), 1987–1994, doi:10.1029/JA085iA05p01987.

Shepherd, S. G. (2014), Altitude-adjusted corrected geomagnetic coordinates: Definition and functional approximations, *Journal of Geophysical Research: Space Physics*, *119*(9), 7501–7521, doi:10.1002/2014JA020264.

Shore, R. M., M. P. Freeman, J. A. Wild, and J. W. Gjerloev (2017), A high-resolution model of the external and induced magnetic field at the Earth's surface in the Northern Hemisphere, *Journal of Geophysical Research: Space Physics*, *122*(2), 2016JA023682, doi:10.1002/2016JA023682.

Sofko, G. J., R. Greenwald, and W. Bristow (1995), Direct determination of large-scale magnetospheric field-aligned currents with SuperDARN, *Geophysical Research Letters*, *22*(15), 2041–2044, doi:10.1029/95GL01317.

Stolle, C., R. Floberghagen, H. Lühr, S. Maus, D. J. Knudsen, P. Alken, E. Doornbos, B. Hamilton, A. W. P. Thomson, and P. N. Visser (2013), Space Weather opportunities from the Swarm mission including near real time applications, *Earth, Planets and Space*, *65*(11), 17, doi:10.5047/eps.2013.10.002.

Stolle, C., G. Kervalishvili, and J. Rauberg (2017), Swarm L2 FAC-dual product description, *Tech. Rep. SW-TR-GFZ-GS-008*, GFZ.

Streltsov, A. V., and W. Lotko (2004), Multiscale electrodynamics of the ionosphere-magnetosphere system, *Journal of Geophysical Research: Space Physics*, *109*(A9), A09214, doi:10.1029/2004JA010457.

Sugiura, M., N. C. Maynard, W. H. Farthing, J. P. Heppner, B. G. Ledley, and L. J. Cahill (1982), Initial results on the correlation between the magnetic and electric fields observed from the DE-2 satellite in the field-aligned current regions, *Geophysical Research Letters*, *9*(9), 985–988, doi:10.1029/GL009i009p00985.

Swarm Level 2 Processing System Consortium (2012), Detailed Processing Model (DPM) FAC, Swarm Level 2 Processing System, *Tech. Rep. SW-DS-GFZ-GS-0002*.

Vasyliunas, V. M. (1979), Interaction between the magnetospheric boundary layers and the ionosphere, in *Proceedings of the Magnetospheric Boundary Layers Conference*, *ESA Special Publication*, vol. 148, edited by B. Battrick, J. Mort, G. Haerendel, and J. Ortner, pp. 387–393.

Vennerstrøm, S., T. Moretto, N. Olsen, E. Friis-Christensen, A. M. Stampe, and J. F. Watermann (2002), Field-aligned currents in the dayside cusp and polar cap region during northward IMF, *Journal of Geophysical Research: Space Physics*, *107*(A8), SMP 18–1–SMP 18–5, doi:10.1029/2001JA009162.

Wang, C., I. G. Rosen, B. T. Tsurutani, O. P. Verkhoglyadova, X. Meng, and A. J. Mannucci (2016), Statistical characterization of ionosphere anomalies and their relationship to space weather events, *J. Space Weather Space Clim.*, *6*(A5), doi:10.1051/swsc/2015046.

Wang, H., H. Lhr, and S. Y. Ma (2005), Solar zenith angle and merging electric field control of field-aligned currents: A statistical study of the Southern Hemisphere, *Journal of Geophysical Research: Space Physics*, *110*(A3), A03306, doi:10.1029/2004JA010530.

Waters, C. L., B. J. Anderson, and K. Liou (2001), Estimation of global field aligned currents using the iridium System magnetometer data, *Geophysical Research Letters*, *28*(11), 2165–2168, doi:10.1029/2000GL012725.

Weimer, D. R. (2001), Maps of ionospheric field-aligned currents as a function of the interplanetary magnetic field derived from Dynamics Explorer 2 data, *Journal of Geophysical Research: Space Physics*, *106*(A7), 12,889–12,902, doi:10.1029/2000JA000295.

Weimer, D. R. (2005), Improved ionospheric electrodynamic models and application to calculating joule heating rates, *Journal of Geophysical Research: Space Physics*, *110*(A5), A05306, doi:10.1029/2004JA010884.

Wing, S., S.-i. Ohtani, P. T. Newell, T. Higuchi, G. Ueno, and J. M. Weygand (2010), Dayside field-aligned current source regions, *Journal of Geophysical Research: Space Physics*, *115*(A12), A12215, doi:10.1029/2010JA015837.

Zhang, B., R. H. Varney, W. Lotko, O. J. Brambles, W. Wang, J. Lei, M. Wiltberger, and J. G. Lyon (2015), Pathways of F region thermospheric mass density enhancement via soft electron precipitation, *Journal of Geophysical Research: Space Physics*, *120*(7), 2015JA020999, doi:10.1002/2015JA020999.

Zmuda, A. J., J. H. Martin, and F. T. Heuring (1966), Transverse magnetic disturbances at 1100 kilometers in the auroral region, *Journal of Geophysical Research*, *71*(21), 5033–5045, doi:10.1029/JZ071i021p05033.

Zou, Y., Y. Nishimura, J. K. Burchill, D. J. Knudsen, L. R. Lyons, K. Shiokawa, S. Buchert, S. Chen, M. J. Nicolls, J. M. Ruohoniemi, K. A. McWilliams, and N. Nishitani (2016), Localized field-aligned currents in the polar cap associated with airglow patches, *Journal of Geophysical Research: Space Physics*, *121*(10), 2016JA022665, doi: 10.1002/2016JA022665.

Table 1. Scale sizes used to determine multi-scale FAC characteristics and relationships

Data source	**Filter period** [s]	**Scale size** ([km] MLAT)
Swarm A (single-satellite estimate)	No filter	7.5
Swarm A (single-satellite estimate)	8	∼50
Swarm A (single-satellite estimate)	20	∼150
Swarm AC (dual-satellite estimate)	20 (low-pass)[a]	∼150
Swarm A (single-satellite estimate)	48	∼350
AMPERE	N/A	∼350

[a]Filtering applied as part of Swarm science team preparation of Swarm dual-satellite Level 2 data products [*Olsen et al.*, 2013; *Stolle et al.*, 2017].

Table 2. Summer-to-winter Ratio Estimates

Study	**Summer-to-winter ratio**	**Notes**
Fujii et al. [1981]	∼2.0	TRIAD satellite data large-scale FACs (2 hr MLT resolution)
Papitashvili et al. [2002]	∼1.35	Model based on Øersted and Magsat satellite dat 5° MLAT × 20 min MLT resolution
Christiansen et al. [2002]	∼1.5-1.8	Øersted and Magsat satellite data 1° MLAT × 20 min MLT resolution incomplete MLT coverage
Ridley [2007]	∼1.6	Model results large-scale FACs
Juusola et al. [2009]	∼1.4	CHAMP/SECS method large-scale FACs
This study Swarm A 50 km scale Swarm A 150 km scale Swarm AC Swarm A 350 km scale AMPERE	 ∼1.27 ∼1.36 ∼1.36 ∼1.34 ∼1.34	Swarm and AMPERE data, 1° × variable MLT r

Table 3. Summary of findings regarding multi-scale characteristics and controlling parameters and primary figures providing support

Characteristic/Controlling parameter	**Multi-scale significance**	
IMF clock angle	Increased influence of small and mesoscale FACs when IMF is not dominated by southward component.	
Correlation	Dawn and dusk are the only local time sectors where the small and large-scales have, on average, similar forms. Noon local time exhibits very limited agreement between multi-scale FACs.	
Degree of Departure from nominal R1/R2 system	Departure is greatest along the noon-midnight local time meridian. To accurately model small and mesoscale FACs both improved understanding of the physics of FACs along this meridian *and* increased model resolution are needed.	

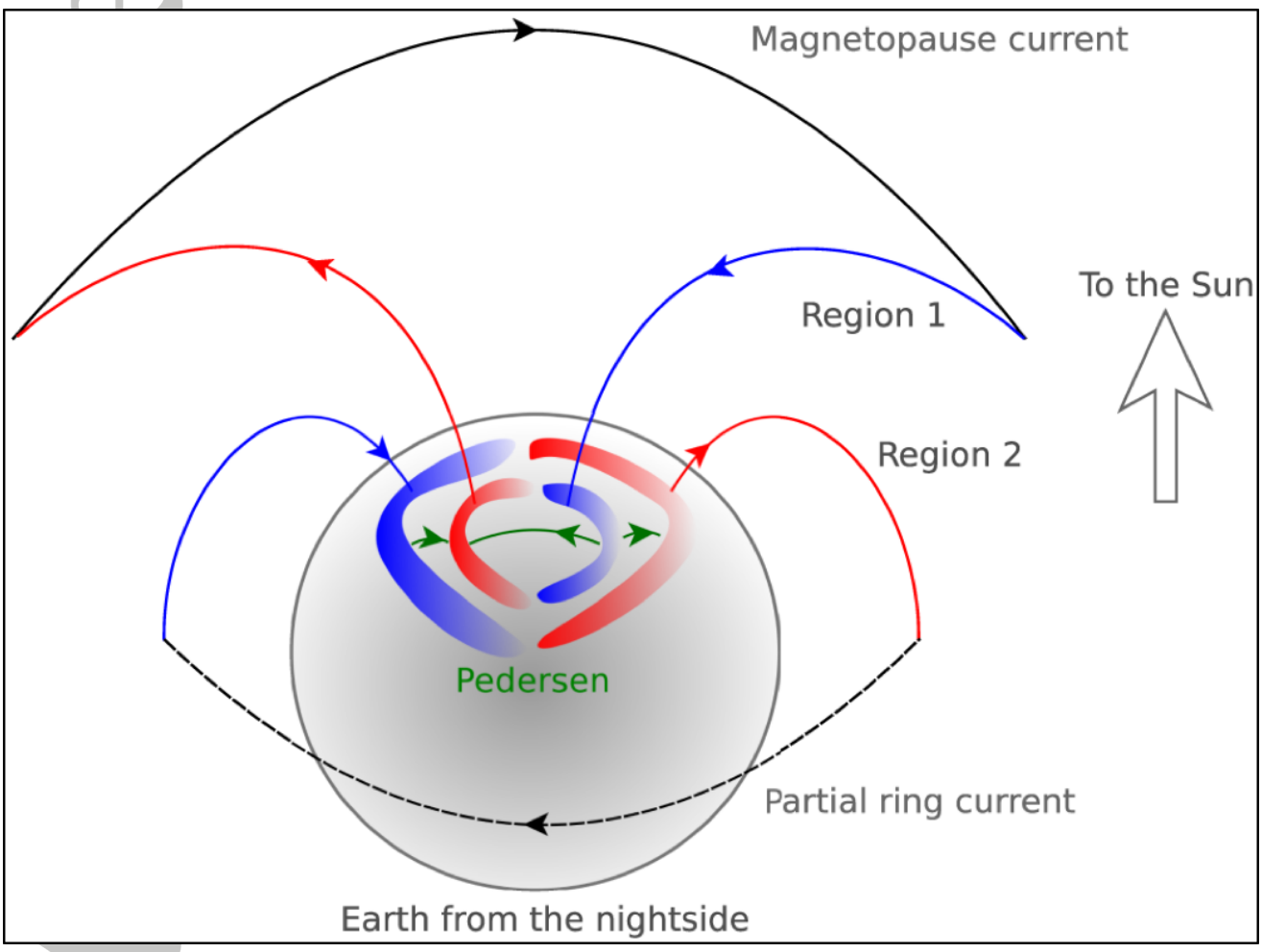

Figure 1. The global layout of the northern hemispheric magnetospheric current systems of the Earth, including the Region 1 and 2 currents (blue and red and downward and upward, respectively), magnetopause current (black), partial ring current (black dashed), and ionospheric Pedersen currents flowing across the polar cap (green). Figure reproduced with permission from *Carter et al.* [2016].

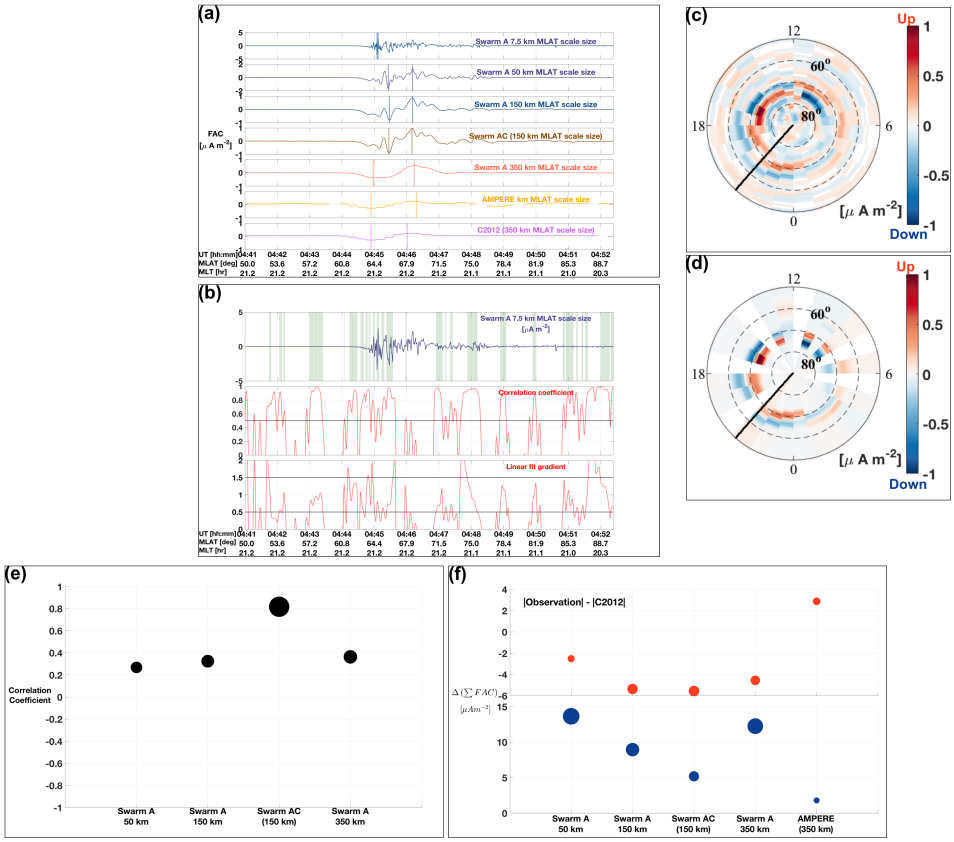

Figure 2. Swarm northern hemisphere pass on February 23, 2015 (04:41-04:52 UT), shown as a representative example. (a) FAC density data investigated in this work: Swarm A single-satellite (7.5, 50, 150, and 350 km scale sizes shown), Swarm AC dual-satellite, and AMPERE (sampled along the Swarm orbit). Color-coordinated vertical bars on each panel indicate the MLAT of the maximum and minimum FACs. (b) *Forsyth et al.* [2017] criteria to determine quality single-satellite FAC estimates. The top panel shows the Swarm A 1 Hz FAC density estimates. The middle and bottom panels show the correlation coefficient and linear fit gradient calculated using the 13 sec frequency filter window for each data point (see text), respectively. Black horizontal lines indicate the thresholds applied in this work ($\geq$0.5 correlation, and 0.5$\leq$ linear fit gradient $\leq$ 1.5). Data points meeting the criteria used in this work are indicated by green vertical bars in the top panel. All other data points from each data set (Swarm A, Swarm AC, and AMPERE) are excluded from our analyses. (c) Global, northern hemisphere, high-latitude AMPERE FAC distribution. Median FACs for the time period of the Swarm pass (04:41-04:52 UT) are shown. Superimposed black points indicate the Swarm pass. (d) Same as (c) except the *Clausen et al.* [2012] FAC fits to the AMPERE data are displayed. MLT sectors where the fit is unreliable are removed from the plot and excluded from our analyses. These data are compared with the FAC data shown in (a) to compute degree of departure measures. (e) Correlations between Swarm and AMPERE data. Data point sizes and locations on the y-axis reflect the magnitude of the correlation. (f) Difference between the pass-summed upward (red, top panel) and downward (blue, bottom panel) FACs. Differences are computed between the absolute values of the FAC observations (Swarm and AMPERE) and the C2012 FACs. Data point sizes and locations on the y-axis reflect the magnitude of the departure of the observations from the fit.

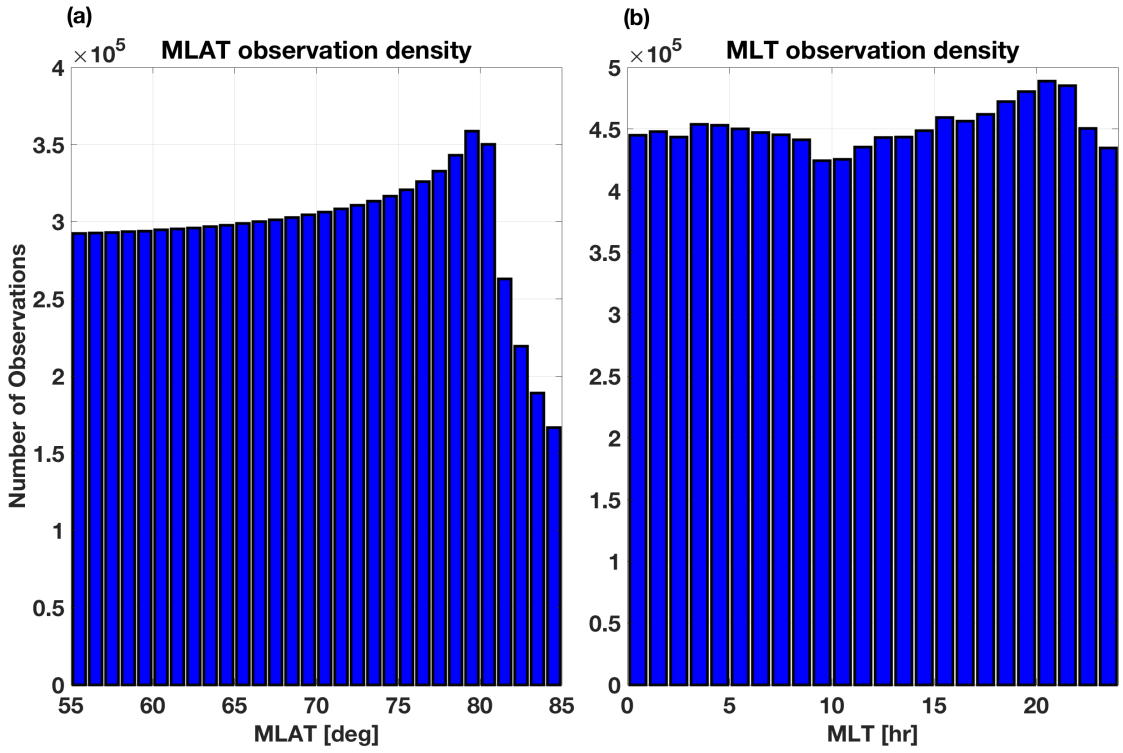

Figure 3. Observation occurrence statistics as a function of altitude adjusted corrected geomagnetic (AACGM) coordinates: (a) MLAT and (b) MLT. The full database of FAC observations is used.

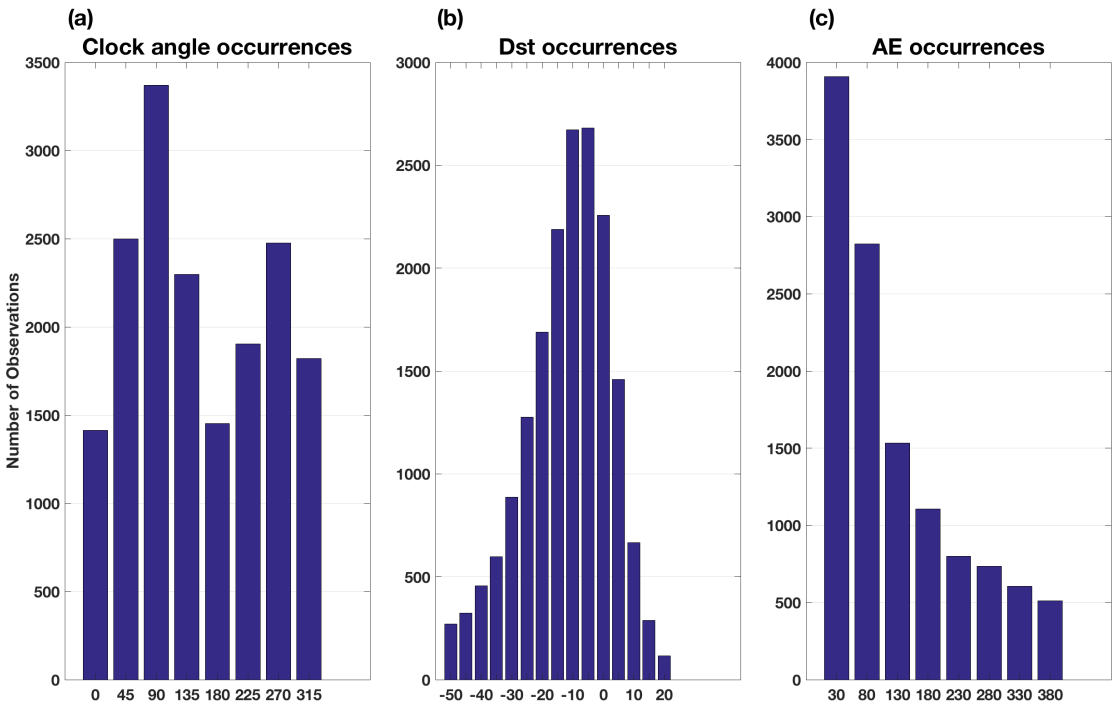

Figure 4. IMF and geomagnetic activity index occurrence statistics corresponding to the FAC database used in this work. (a) IMF clock angle; (b) the disturbance storm time index (Dst); and (c) the auroral electrojet index (AE). A single value of each parameter is recorded for each Swarm pass. The median value across the time of the Swarm pass is calculated from 5 min resolution data.

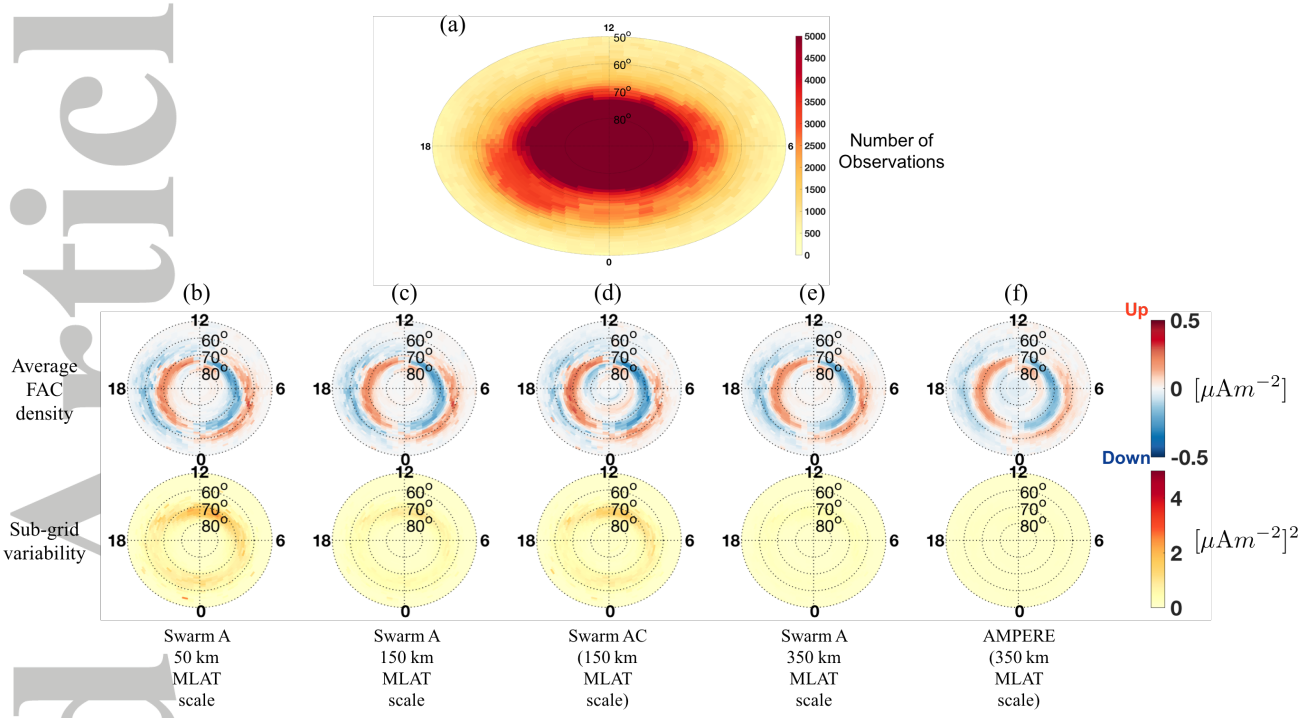

Figure 5. Northern Hemisphere polar distributions of FAC density in AACGM MLAT-MLT coordinates: (a) Observation density, (b-f) average FAC densities (top panel) and sub-grid variability (bottom panel). (b) Swarm A 50 km, (c) Swarm A 150 km, (d) Swarm AC (150 km), (e) Swarm A 350 km, and (f) AMPERE (350 km). Data are shown on an equal area grid in AACGM MLAT-MLT coordinates with noon MLT to the top of each polar plot and a low-latitude limit of 50°. Positive FACs are oriented away from the ionosphere (up, shown in red) and negative FACs are toward the ionosphere (down, shown in blue).

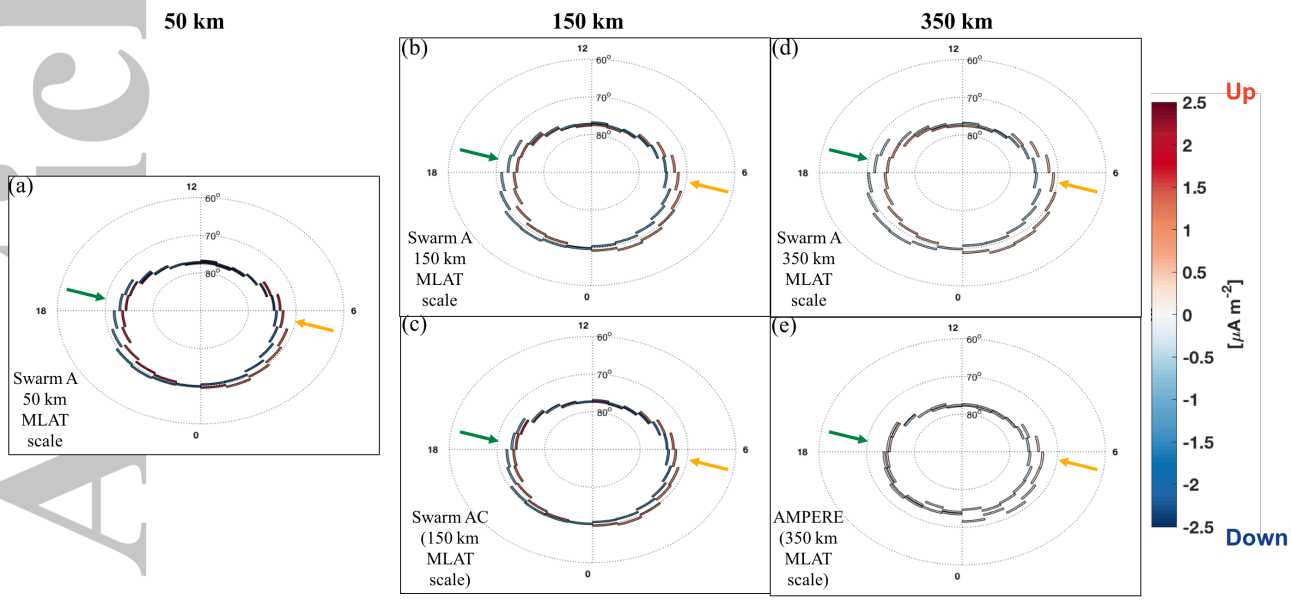

Figure 6. MLAT-MLT location of average peak FACs for all scales. The peak FACs (both positive and negative), their MLAT locations, and the median MLT value for each Swarm pass are accumulated. The average peak FACs and MLAT locations are shown here, and 1 h MLT bins are used. Colors indicate average peak densities. Positive FACs are oriented away from the ionosphere (up, shown in red) and negative FACs are toward the ionosphere (down, shown in blue). Different scale sizes are shown on different polar plots: (a) Swarm A 50 km; (b) Swarm A 150 km; (c) Swarm AC; (d) Swarm A 350 km; and (d) AMPERE. Green and orange arrows point out specific MLT locations discussed in the text and referenced in Figure 7.

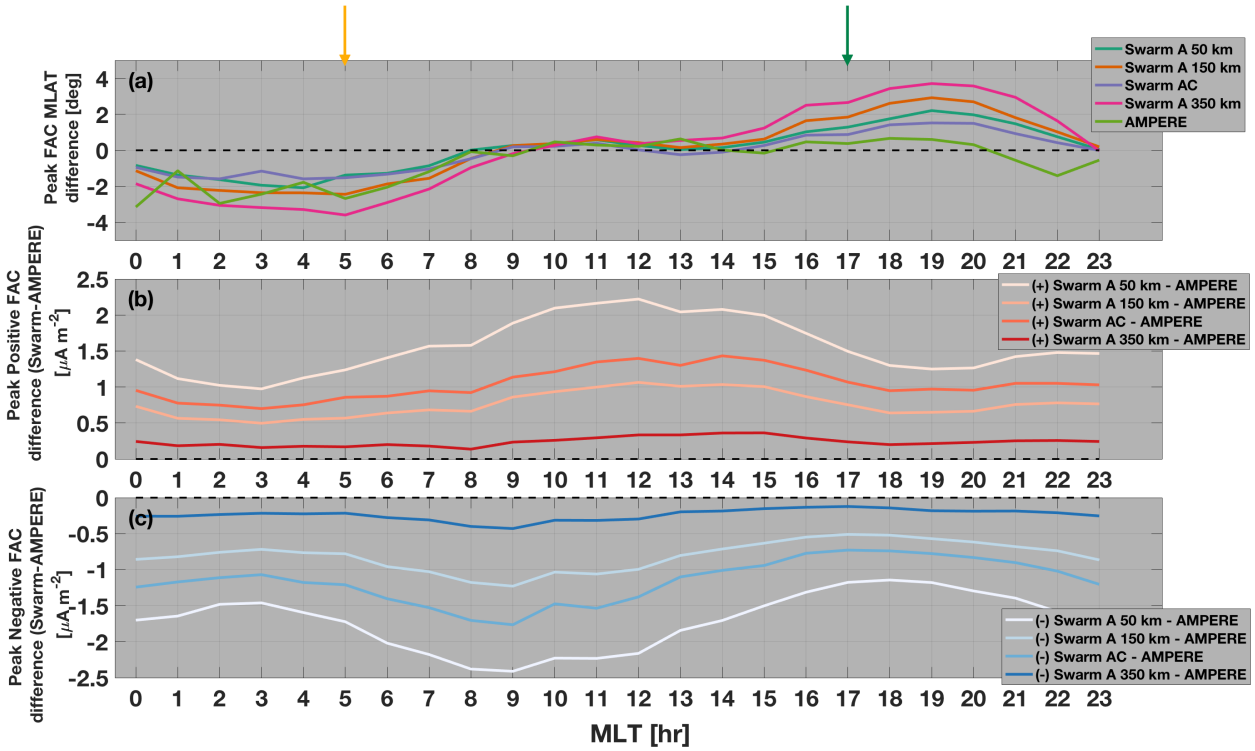

Figure 7. Quantitative differences of peak FACs as a function of MLT. (a) Difference in MLAT location of peak FACs $\left(\mathrm{MLAT}_{\text{peak }+J_r} - \mathrm{MLAT}_{\text{peak }-J_r}\right)$ for each scale size. Difference between Swarm and AMPERE FACs for (b) peak positive FACs $\left(\text{peak } +J_{r,\text{ Swarm}} - \text{peak } +J_{r,\text{ AMPERE}}\right)$ and (c) peak negative FACs $\left(\left|\text{peak } -J_{r,\text{ Swarm}}\right| - \left|\text{peak } -J_{r,\text{ AMPERE}}\right|\right)$. Green and orange arrows point out specific MLT locations discussed in the text and referenced in Figure 6.

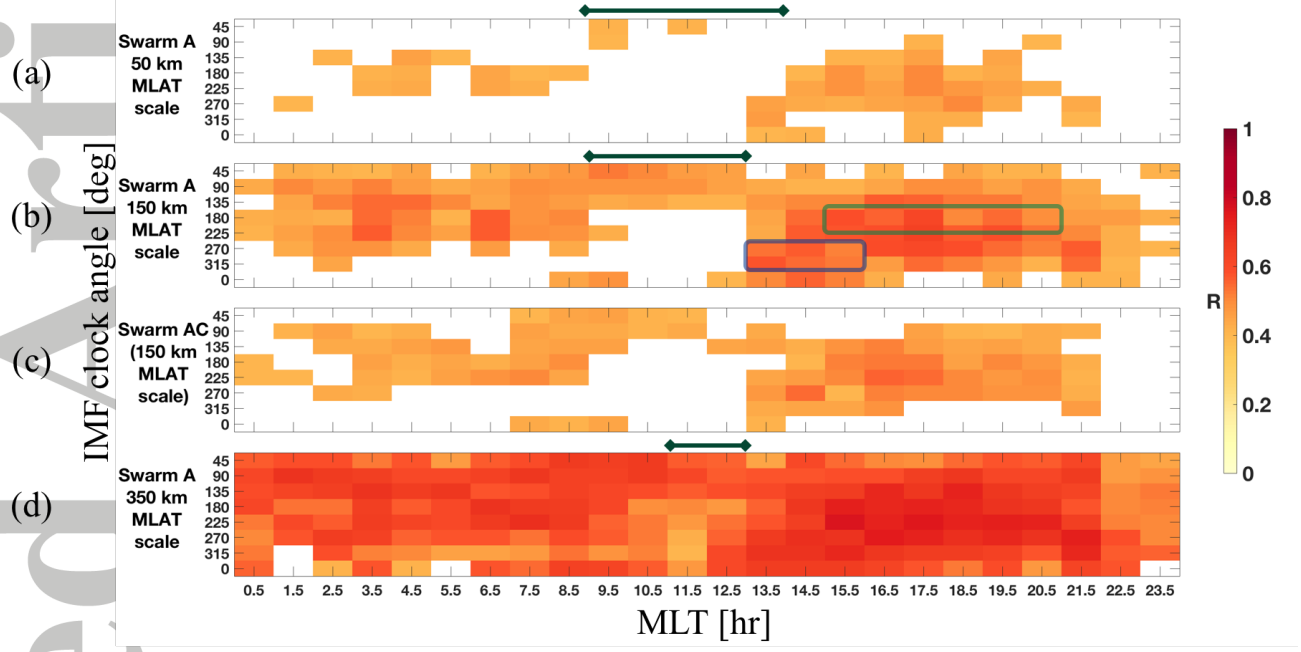

Figure 8. Average correlation coefficients between Swarm and AMPERE as a function of MLT and IMF clock angle: (a) Swarm A 50 km, (b) Swarm A 150 km, (c) Swarm AC, and (d) Swarm A 350 km. 1 h MLT (x-axis) and 45° clock angle (y-axis) bins are used. Average correlation coefficients are calculated in each bin. Bins with average correlations < 0.4 are left empty.

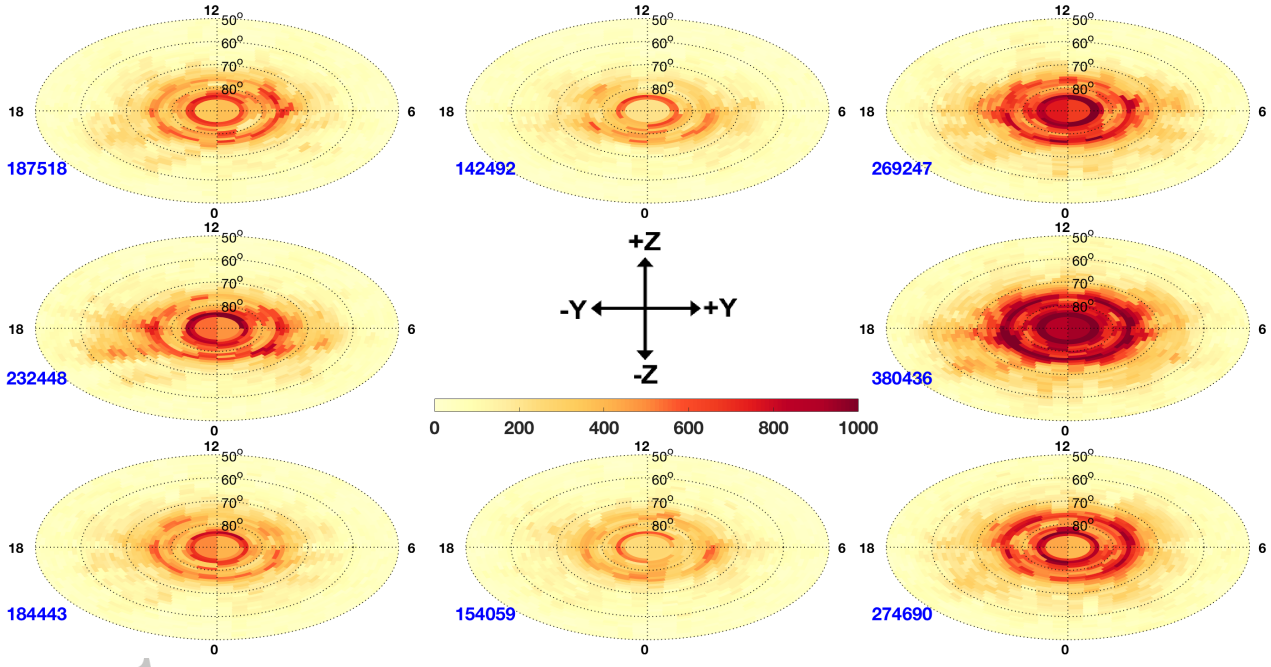

Figure 9. Northern hemisphere distributions of observation density as a function of IMF clock angle. All data have been binned onto an equal area MLAT-MLT grid in AACGM coordinates. The MLAT resolution is 1°, and the MLT resolution is variable to yield equal area bins (0.28 hours at 50° MLAT to 2.18 hours at 85°). Dashed rings show MLATs at 10° increments, extending down to the low-latitude limit of 50°. The data plotted are number of observations, and the blue values to the bottom left of each plot are the total number of observations in that IMF clock angle bin. Noon MLT is at the top of each polar plot with dawn to the right. Clock angles increase in 45° increments in the clockwise direction.

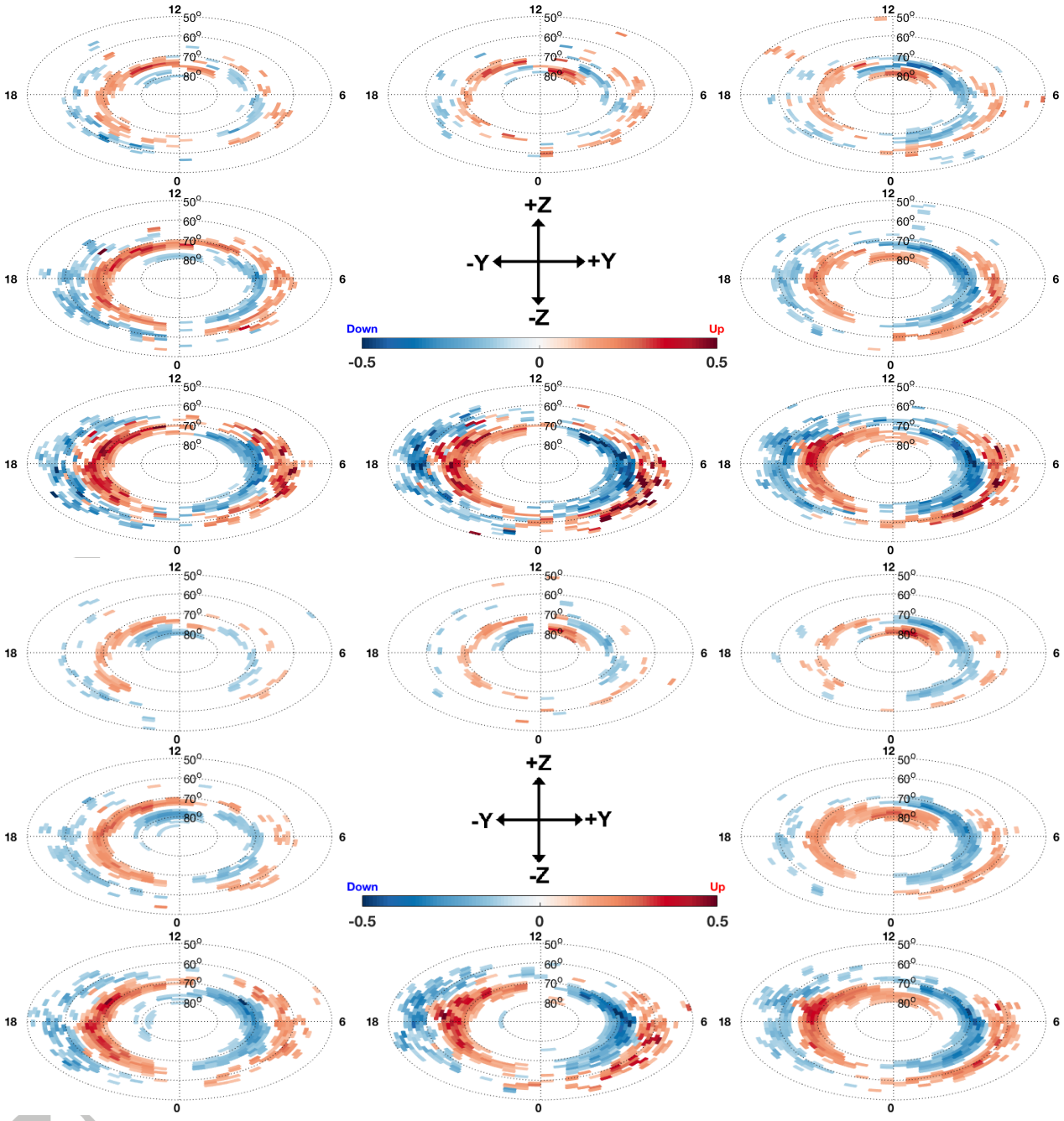

Figure 10. Northern hemisphere distributions of 350 km scale size FACs as a function of IMF clock angle for two different data sets: (top) Swarm A and (bottom) AMPERE. All data have been binned onto an equal area MLAT-MLT grid in AACGM coordinates. The MLAT resolution is 1°, and the MLT resolution is variable to yield equal area bins (0.28 hours at 50° MLAT to 2.18 hours at 85°). Dashed rings show MLATs at 10° increments, extending down to the low-latitude limit of 50°. The data plotted are FAC density [μA m^{-2}]. Noon MLT is at the top of each polar plot with dawn to the right. Clock angles increase in 45° increments in the clockwise direction. FACs shown in red are upward (away from the ionosphere), and those shown in blue are downward (toward the ionosphere). Bins in which the average FAC density is strictly less than 0.1 μA m^{-2} are left empty.

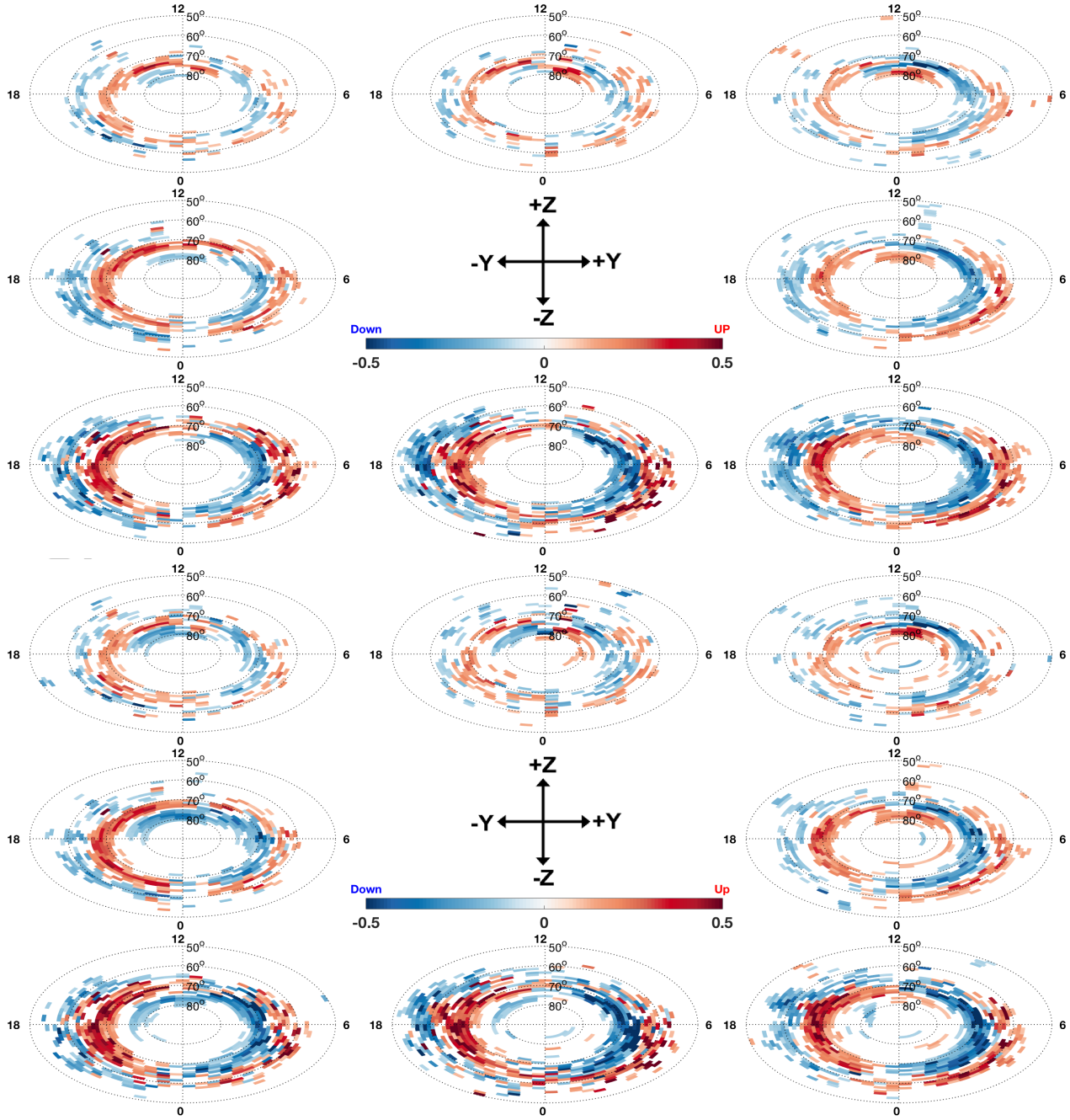

Figure 11. Northern hemisphere distributions of 150 km scale size FACs, following the format of Figure 10. (top) Swarm A (single-satellite estimate) and (bottom) Swarm AC (dual-satellite estimate).

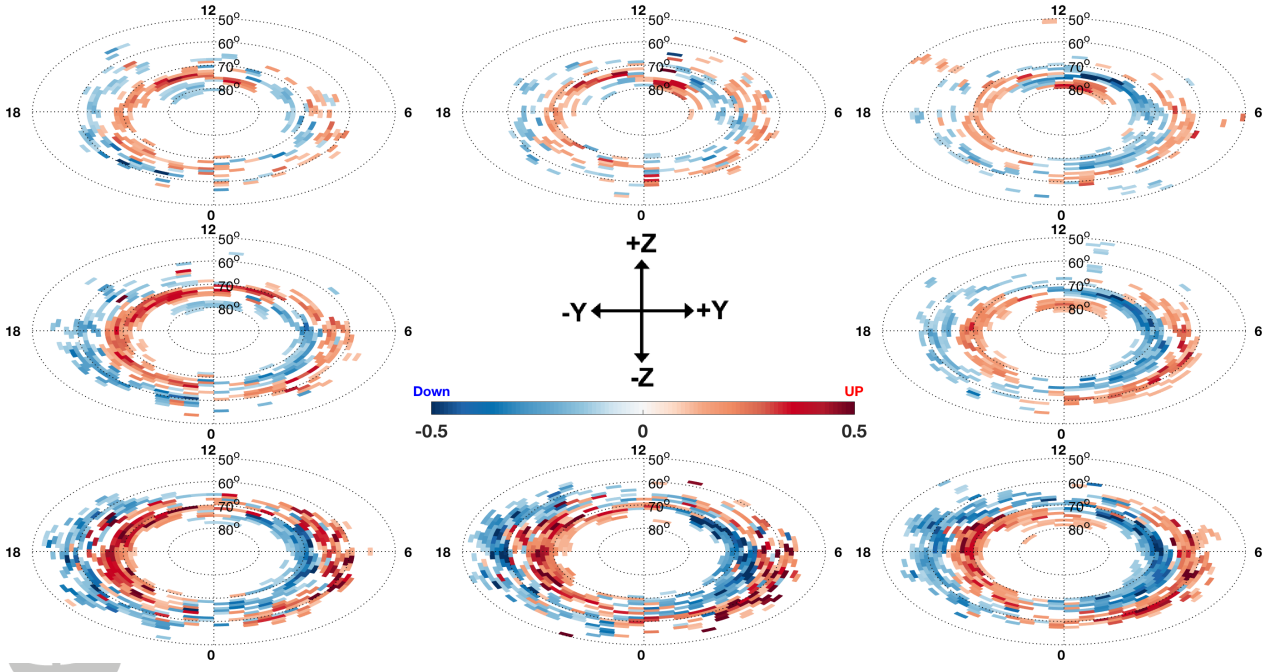

Figure 12. Northern hemisphere distributions of 50 km scale size FACs, following the format of Figure 10. Only Swarm single-satellite estimates are capable of providing FAC data at these scales. Data shown are from Swarm A.

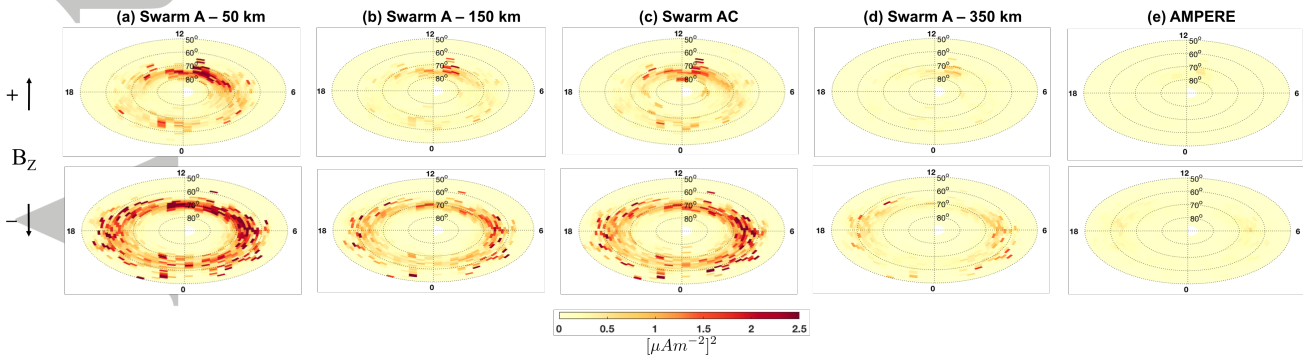

Figure 13. Northern hemisphere distributions of sub-grid level variability during purely northward (clock angle bin $0 \pm 22.5°$) and southward ($90 \pm 22.5°$) IMF conditions. Distributions are shown for: Swarm A at 50 km (a), 150 km (b), and 350 km (d) scale size, Swarm AC (c), and AMPERE (e). Polar plot formatting follows Figure 10.

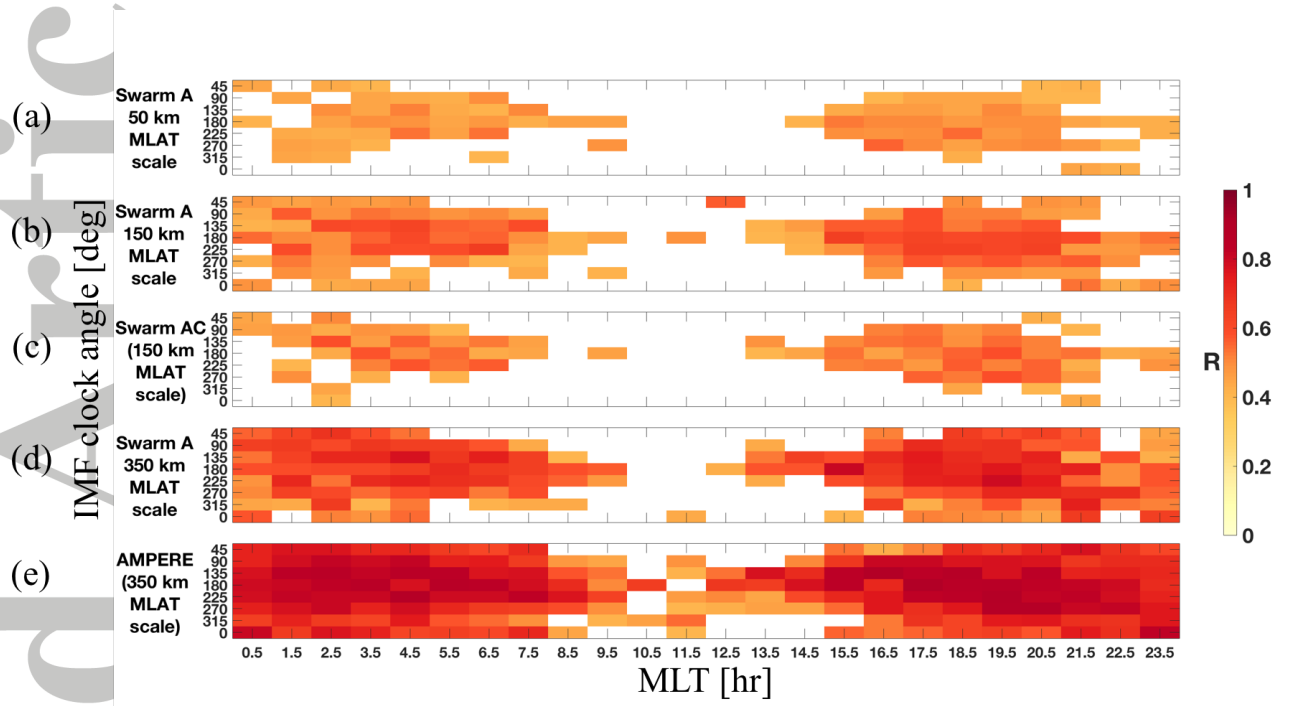

Figure 14. Average correlation coefficients between observed and C2012 FACs as a function of MLT and IMF clock angle: (a) Swarm A 50 km, (b) Swarm A 150 km, (c) Swarm AC, (d) Swarm A 350 km, and (e) AMPERE. 1 h MLT (x-axis) and 45° clock angle (y-axis) bins are used. Average correlation coefficients are calculated in each bin. Bins with average correlations < 0.4 are left empty.

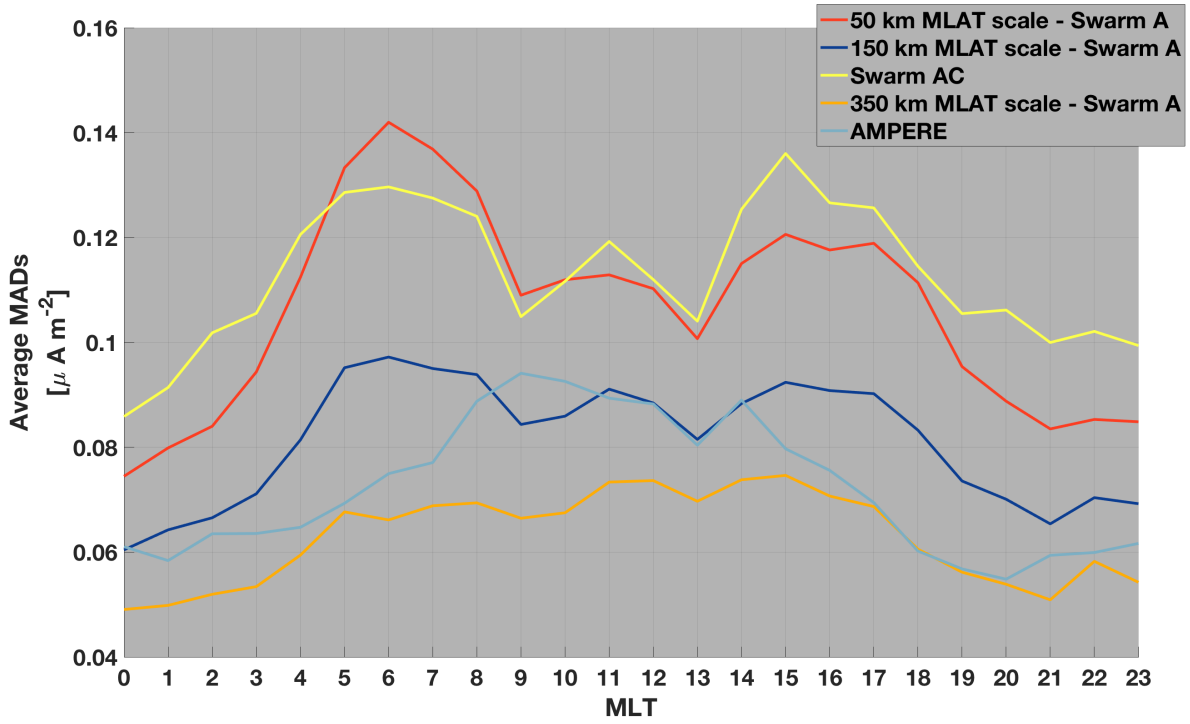

Figure 15. Average median absolute deviations (MADs) for observed FACs compared with C2012 FACs as a function of MLT: (red) Swarm A 50 km, (dark blue) Swarm A 150 km, (yellow) Swarm AC, (orange) Swarm A 350 km, and (light blue) AMPERE. 1 h MLT (x-axis) bins are used.

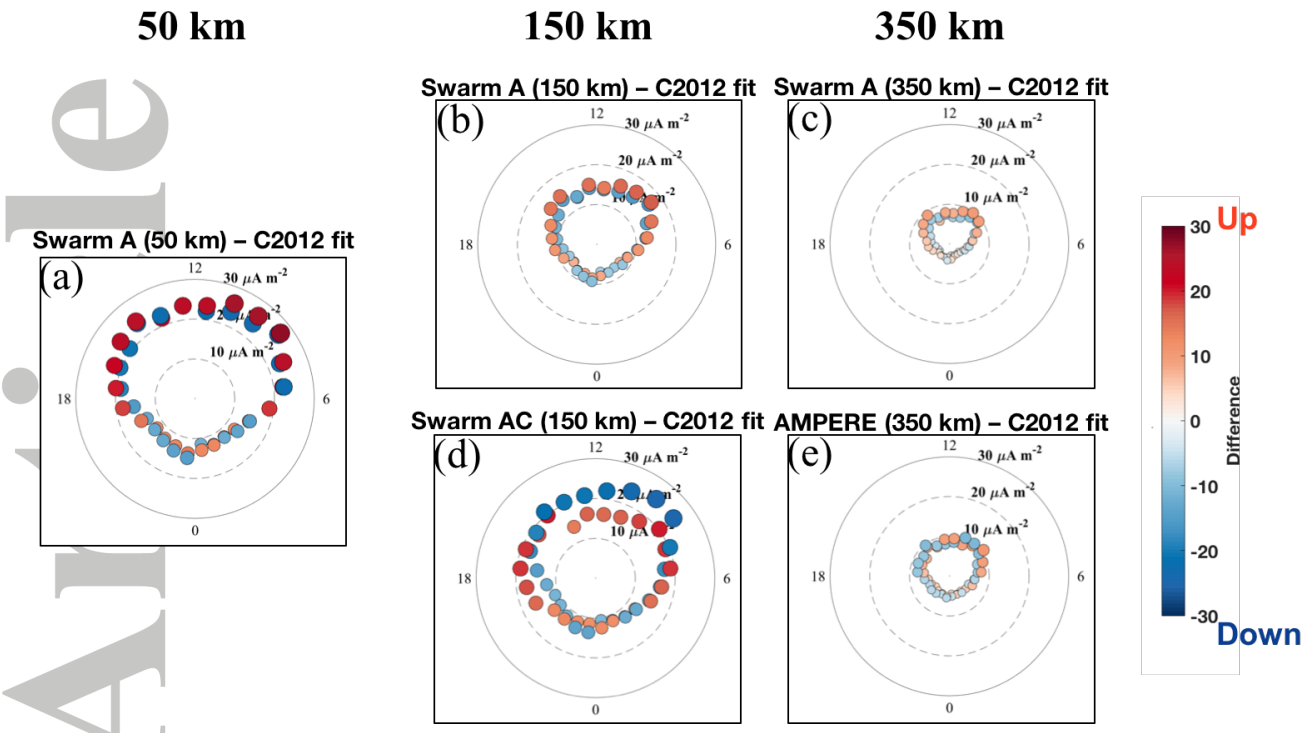

Figure 16. Difference between the summed FACs as a function of MLT. Differences are separately calculated for positive (upward FAC, shown in red) and negative (downward FAC, shown in blue) currents and are computed as the median of all pass-summed FACs at a given scale in a 1 h MLT sector minus the C2012 FACs (see Equations 2 and 3 in text). (a) Swarm A 50 km − C2012, (a) Swarm A 150 km − C2012, (a) Swarm AC − C2012, (a) Swarm A 350 km − C2012, and (e) AMPERE − C2012. Polar plots show MLT-difference, where the distance from the pole indicates the magnitude of the observation-C2012 difference. Note the change from previous polar plots, which showed MLT-MLAT distributions. Dashed rings show difference magnitudes at 10 μA m^{-2} increments, extending to the greatest magnitude plotted of 30 μA m^{-2}. The size and color of the data points further indicate the magnitude of the differences for clarity, and the larger difference is plotted on top in MLT locations where the positive and negative data points overlap.

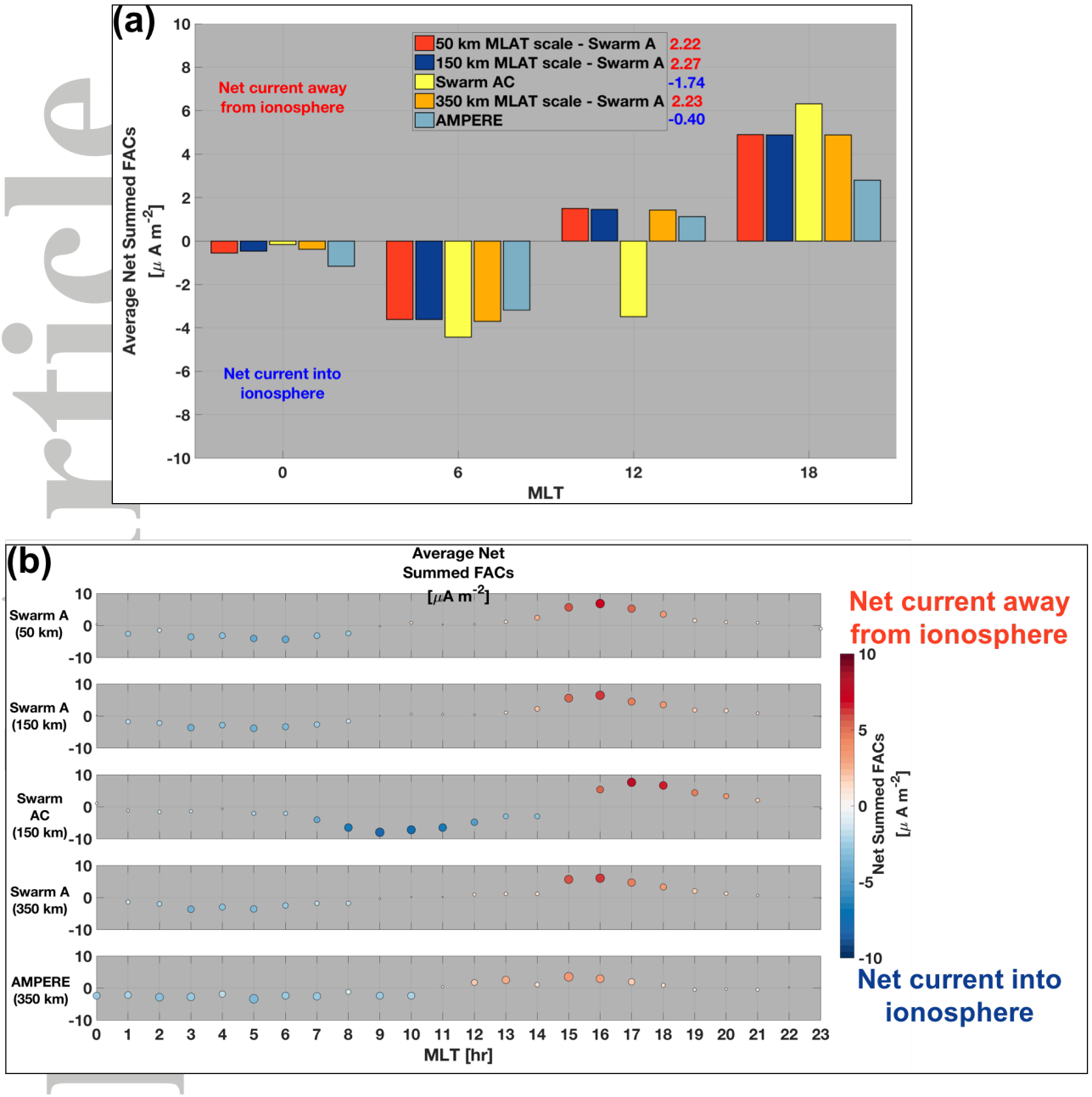

Figure 17. MLT dependence of the average net summed FACs. The averages are calculated for two different MLT bins: (a) four, six hour bins (midnight: 2100-0300, dawn: 0300-0900, noon: 0900-1500, and dusk: 1500-2100) to study the four key MLT sectors (midnight, dawn, noon, and dusk), and b) one hour bins to gain more granularity in the MLT behavior. Figure 17a shows the results for each scale size as a different bar for each of the four MLT sectors. Positive values indicate net currents flowing out of the ionosphere and negative values are net currents flowing in. Values to the right of the legend indicate the total global net current for each set of data. Figure 17b shows the net FACs in one hour bins with a different panel for each data set. The y-axis location, size, and color of the data points indicate the net currents.